remote sensing

MDPI

Article

A Decadal Total Suspended Solids Dataset for China's Coastal Waters Reconstructed from Sentinel-2 Imagery Using a Spatiotemporal Graph Neural Network

Yan Gu [1,*], Junjie Rui [1], Heyang Shi [1], Chuhan Zhang [1] and Ya Ping Wang [2]

[1] School of Internet of Things, Nanjing University of Posts and Telecommunications, Nanjing 210023, China; 1024072109@njupt.edu.cn (J.R.); 1025071812@njupt.edu.cn (H.S.); b22100505@njupt.edu.cn (C.Z.)
[2] School of Geography and Ocean Science, Nanjing University, Nanjing 210023, China; ypwang@nju.edu.cn
* Correspondence: guyan@njupt.edu.cn

Highlights

What are the main findings?

- A spatiotemporal graph neural network framework is developed for satellite-based total suspended solids (TSS) retrieval by integrating spatial dependencies and temporal variations.
- A monthly TSS concentration dataset from 2016 to 2025 is reconstructed for China's coastal waters using Sentinel-2 observations and spatiotemporal deep learning.
- The reconstructed dataset accurately captures the spatial distribution, seasonal variability, and interannual dynamics of coastal suspended sediments.

What are the implications of the main findings?

- The proposed STGNN-TSS framework demonstrates the potential of spatiotemporal learning methods for large-scale and long-term coastal water quality monitoring.
- The reconstructed TSS dataset provides valuable information for understanding coastal sediment dynamics and supporting marine environmental management.

Abstract

Total suspended solids (TSS) are a key indicator of coastal water quality and sediment dynamics, yet their long-term spatiotemporal variability remains insufficiently characterized at large spatial scales. In this study, a decade-long (2016–2025) TSS dataset for China's coastal waters was reconstructed from Sentinel-2 multispectral imagery using a spatiotemporal graph neural network (STGNN-TSS), which integrates graph attention networks with temporal sequence modeling. The model was trained using satellite-derived reference TSS observations and evaluated using spatially separated test samples and comparative experiments. During relatively stable seasonal conditions, STGNN-TSS achieved an R^2 of 0.739, an RMSE of 3.924 mg L^{-1}, and an MAE of 1.907 mg L^{-1} across China's coastal waters. The reconstructed products for other years showed consistent spatial patterns with independent satellite-derived SPM products, with Spearman correlation coefficients ranging from 0.738 to 0.891. Based on the reconstructed dataset, TSS exhibited a persistent "high-inshore, low-offshore" spatial pattern with pronounced regional differences among northern shallow seas, major estuarine systems, and southern coastal waters. Seasonal variations were identified, characterized by elevated TSS concentrations in winter and reduced concentrations in summer. Interannual variability during 2016–2025 showed an increasing trend before 2020 followed by a general decline, with substantial regional differences in variability intensity. The reconstructed TSS dataset provides a consistent basis

Check for updates

Academic Editor: Teodosio Lacava

Received: 9 August 2026
Revised: 22 October 2026
Accepted: 22 October 2026
Published: 25 October 2026

Copyright: © 2026 by the authors. Licensee MDPI, Basel, Switzerland. This article is an open access article distributed under the terms and conditions of the Creative Commons Attribution (CC BY) license.

for investigating long-term suspended sediment dynamics and supports large-scale coastal environmental monitoring and management.

Keywords: total suspended solids (TSS); coastal waters; spatiotemporal modeling; graph neural network; Sentinel-2

1. Introduction

Total suspended solids (TSS) is a key water quality parameter that influences water turbidity, underwater light availability, and overall aquatic environmental conditions [1,2]. In shallow marine environments, TSS dynamics are primarily controlled by a combination of riverine sediment input, tidal and wave forcing, sediment resuspension, bathymetry, and anthropogenic activities [3–6]. These interacting factors result in pronounced spatial heterogeneity and strong temporal variability [7,8], making long-term, large-scale monitoring essential for understanding coastal environmental processes and ecosystem health.

Traditional TSS measurements primarily rely on field sampling, which is constrained by limited spatial coverage, low temporal frequency, and high operational costs [9,10]. In contrast, satellite remote sensing provides an efficient and cost-effective alternative owing to its wide spatial coverage, high revisit frequency, and consistent observation capability [11,12]. Consequently, it has become one of the most widely adopted approaches for monitoring suspended sediments in aquatic environments [13–16].

Early studies using medium-and low-resolution sensors, such as MODIS and MERIS, laid the foundation for large-scale TSS estimation [17,18]. For example, Moridnejad et al. [19] applied MODIS imagery combined with artificial neural networks to estimate suspended sediment concentrations in Lake Urmia. With increasing demand for spatial detail, higher-resolution sensors such as Landsat have been widely used to investigate sediment dynamics in lakes, rivers, and coastal systems [20–23]. More recently, improvements in atmospheric correction and water quality retrieval algorithms have further enhanced the applicability of high-resolution satellite data in optically complex coastal waters [24].

With the increasing availability of long-term satellite observations, several studies have attempted to reconstruct multi-year TSS dynamics. Feng et al. [25] analyzed long-term transparency changes in lakes of the Yangtze Plain using MODIS data, while Li et al. [26] and Luo et al. [27] investigated decadal sediment dynamics in the Yellow River and Yangtze River estuaries using Landsat and multi-sensor datasets. Sun et al. [28] further developed a semi-analytical approach to monitor TSS over multiple decades in the Pearl River estuary. These studies demonstrate the feasibility of satellite remote sensing for long-term TSS monitoring. However, most existing studies are limited to regional case studies. Challenges remain in generating spatially continuous, high-resolution, and methodologically consistent TSS products at the national scale.

In parallel, TSS retrieval methods have evolved from empirical and semi-empirical approaches to physics-based models and, more recently, to machine learning and deep learning techniques [29–31]. Given the nonlinear relationship between spectral reflectance and TSS in optically complex waters [32,33], machine learning models, such as random forest and neural networks, have demonstrated improved accuracy and robustness [34,35]. Despite these advances, most existing studies still rely on pixel-wise modeling strategies, which may overlook spatial dependencies and temporal continuity, limiting their performance in large-scale and long-term applications.

To address these limitations, recent studies have explored spatiotemporal deep learning approaches capable of jointly modeling spatial structure and temporal evolution. In particular, spatiotemporal graph neural networks (STGNNs) provide a flexible framework for

modeling spatial dependencies while simultaneously capturing temporal evolution [36–40]. By jointly modeling spatial dependencies and temporal dynamics, these approaches are particularly suitable for complex coastal environments, where sediment transport and redistribution exhibit strong spatiotemporal characteristics [41,42].

Building upon these advances, this study proposes a spatiotemporal deep learning framework to reconstruct a spatially continuous, high-resolution TSS dataset for China's coastal waters from 2016 to 2025. The objectives are to: (1) generate a long-term, high-resolution TSS dataset at the national scale; (2) characterize the spatial distribution, seasonal variability, and interannual dynamics of coastal TSS; and (3) evaluate the applicability of spatiotemporal modeling for large-scale water quality reconstruction. The reconstructed dataset provides new insights into long-term sediment dynamics along China's coastline and provides a scalable framework for large-scale coastal environmental monitoring.

2. Materials and Methods

2.1. Study Area

This study focuses on the coastal waters along the mainland coast of China, spanning from the Liaodong Peninsula in the north to the southern coastal waters of Hainan Island. The study area covers the major marginal seas of China, including the Bohai Sea, Yellow Sea, East China Sea, and the northern South China Sea, extending approximately from 18° to 41°N and 108° to 127°E.

To ensure the spatial integrity of the remote sensing samples and the continuity of coastal hydrodynamic processes, the study domain generally corresponds to the shallow continental shelf, with water depths typically less than 60 m (Figure 1). This configuration encompasses coastal waters strongly influenced by land–sea interactions, including river inputs, tidal mixing, and sediment resuspension.

Coastal waters in this study refer to the overall study domain along the Chinese coast. Within this domain, inshore and offshore waters were distinguished to represent regions with strong and weak terrestrial influence, respectively. Inshore waters are generally characterized by intense riverine input, active sediment resuspension, and high turbidity, whereas offshore waters exhibit relatively low suspended sediment concentrations and more stable hydrodynamic conditions.

2.2. Reference TSS Data

Reference TSS data were obtained from the National Marine Science Data Center of China (https://mds.nmdis.org.cn; access on 12 November 2025), which provides remotely sensed suspended sediment concentration products for the Bohai Sea, Yellow Sea, and East China Sea. The dataset covers approximately 25.02–41.37°N and 116.78–127.71°E, with a spatial resolution of 500 m. The products are provided in NetCDF format and include daily and monthly TSS estimates for representative periods in 2020.

Valid water pixels were identified from the reference TSS products after quality control. Considering the spatial heterogeneity of coastal waters, the study area was divided into spatially stratified regions, and valid pixels were randomly selected within these regions to maintain spatial coverage. A total of 1000 sampling locations were obtained, and their geographic coordinates were recorded as fixed spatial nodes for subsequent observations.

For each available month, TSS values were extracted at the predefined sampling locations from the reference products. Observations affected by invalid quality flags or missing TSS values were removed during dataset construction. The extracted samples contained spatial coordinates, acquisition time, and corresponding TSS measurements at each node.

To represent temporal variations at individual locations, observations from the same spatial nodes were organized according to acquisition time. A three-month sliding temporal

window was applied to construct sequential samples for STGNN-TSS, where each sample consisted of multi-month observations from the same spatial nodes. The corresponding TSS observations were used as supervised targets during model training.

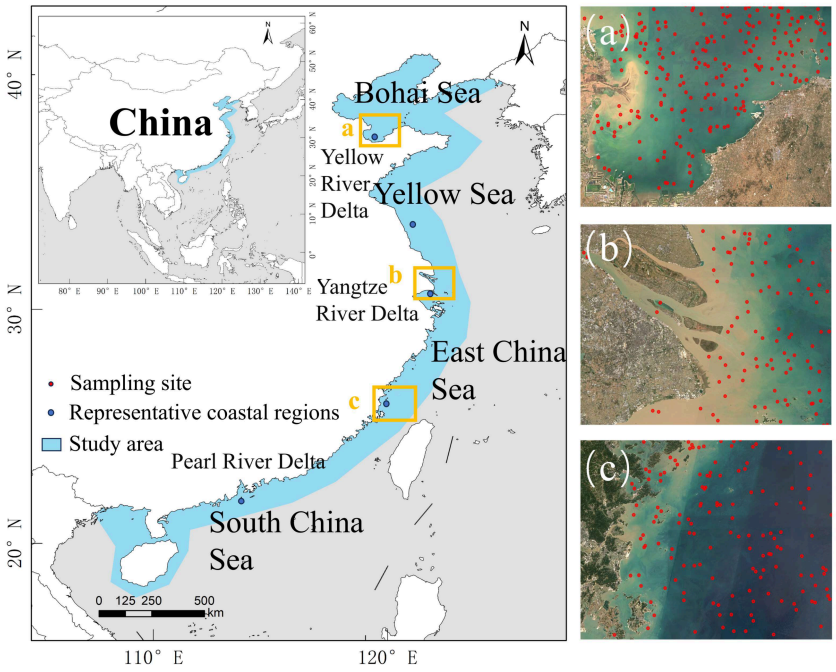


Figure 1. Study area and sampling scheme. The left panel shows the geographic location of China's coastal waters and an overview of the study region. Panels illustrate examples of sampling point distributions in representative coastal areas, including (**a**) Bohai Bay, (**b**) the Yangtze River estuary, and (**c**) the coastal waters of Ningde Port. Red dots indicate example sampling points derived from monthly products of the National Marine Science Data Center, while blue dots denote sampling stations located in typical estuarine and coastal regions and are used for quantitative analysis. The blue shaded area represents the study region, generally corresponding to shallow shelf waters typically with depths less than 60 m along the Chinese coast.

2.3. Satellite Data and Preprocessing

The remote sensing predictors were derived from Sentinel-2 multispectral imagery covering the study region. Sentinel-2 Level-2A surface reflectance products were used, which were generated from Level-1C top-of-atmosphere observations using the Sen2Cor processor. Monthly Sentinel-2 observations were collected for the study period, and images with cloud coverage below 20% were selected to balance the availability of valid observations and the influence of cloud contamination in coastal regions.

Cloud- and cirrus-contaminated pixels were removed using the quality information provided in the Level-2A products, and non-water areas were excluded using water masks. The remaining valid observations were composited into monthly mean reflectance products to reduce short-term observational variability and maintain temporal consistency.

Surface reflectance values from 11 Sentinel-2 spectral bands (B2, B3, B4, B5, B6, B7, B8, B8A, B9, B11, and B12) were extracted at the predefined sampling locations. These bands cover the visible, red-edge, near-infrared, and shortwave infrared regions. During model training, the spectral observations were spatially matched to the 500 m reference TSS pixels to construct input–target pairs.

The extracted spectral features were combined with geographic coordinates and temporal information to construct node-level spatiotemporal inputs. Each sample consisted of multi-band spectral observations from the corresponding spatial nodes within the temporal window, while the matched TSS observations were used as supervised targets for model training.

After model training, the optimized STGNN-TSS model was applied to the monthly Sentinel-2 composites from 2016 to 2025 for long-term reconstruction. Considering the balance between spatial detail and computational efficiency, the monthly Sentinel-2 reflectance composites were resampled to a spatial resolution of 60 m before model inference. The resulting predictions were used to obtain the decadal-scale reconstructed TSS dataset.

2.4. Model Framework

A spatiotemporal graph neural network (STGNN) framework was developed to retrieve TSS across China's coastal waters (Figure 2). The model integrates temporal modeling to capture sequential dependencies and seasonal variability and spatial modeling to represent interactions among neighboring water bodies. This unified framework enables continuous reconstruction of TSS over large spatial and temporal scales.

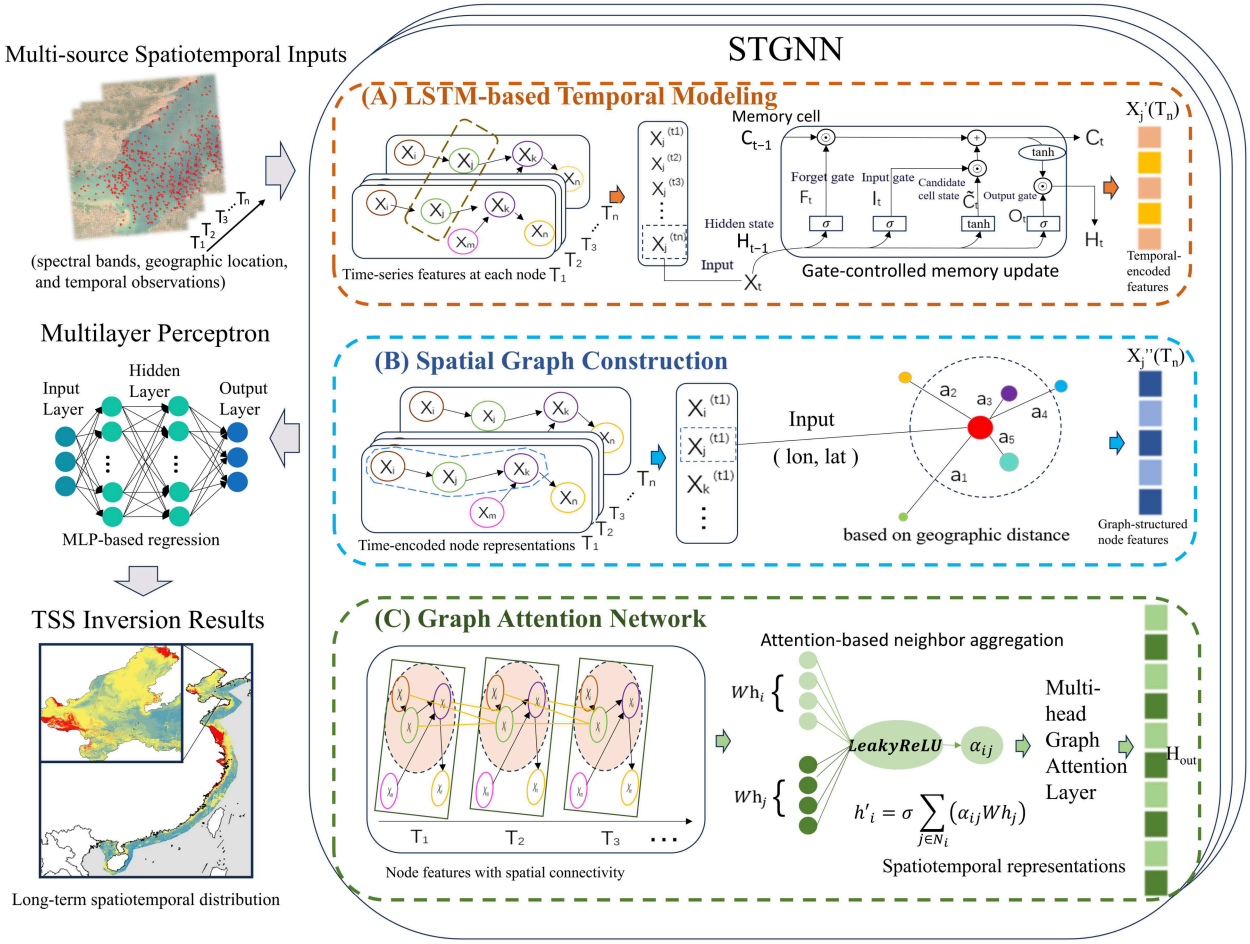


Figure 2. Technical process flowchart of the STGNN-TSS framework. Long-term spatiotemporal sequences consisting of geographic information and TSS observations are input into the STGNN model. Spatial dependencies are captured by a graph attention network (GAT), while temporal dynamics are modeled using an LSTM module. The extracted spatiotemporal features are transformed into TSS estimates through an MLP, and the trained model is further applied to Sentinel-2 imagery for long-term TSS remote sensing inversion.

(1) Multitemporal input construction

Multitemporal satellite observations from 2016 to 2025 were collected to cover China's coastal waters. For each spatial unit, spectral reflectance and derived features were organized into chronological sequences, forming the input sequences for spatiotemporal modeling.

(2) Temporal modeling using LSTM

Long Short-Term Memory (LSTM) networks were employed to capture temporal dependencies in the input sequences. Through its gating mechanisms (input, forget, and output gates), LSTM effectively mitigates the gradient vanishing problem in long sequence modeling [43]. The state update process is formulated as:

$$f_t = \sigma(W_f\,[h_{t-1}, x_t\,] + b_f\,) \tag{1}$$

$$i_t = \sigma(W_i[h_{t-1}, x_t] + b_i) \tag{2}$$

$$c_t = f_t \odot c_{t-1} + i_t \odot tanh(W_c\,[h_{t-1}, x_t\,] + b_c\,) \tag{3}$$

$$o_t = \sigma(W_o[h_{t-1}, x_t] + b_o) \tag{4}$$

$$h_t = o_t \odot tanh(c_t\,) \tag{5}$$

where x_t denotes the input at time step t, while h_t and c_t represent the hidden state and cell state, respectively. f_t, i_t, and o_t denote the forget, input, and output gates. W_f, W_i, W_c, W_o are learnable weight matrices, and b_f, b_i, b_c, b_o are bias vectors. $\sigma(\cdot)$ and $tanh(\cdot)$ denote the sigmoid and hyperbolic tangent activation functions, respectively, and $\odot$ denotes element-wise multiplication. This module represents temporal dependencies within the input sequences, thereby enhancing the model's ability to represent temporal heterogeneity.

(3) Spatial graph construction

In the spatial domain, the study area is represented as a graph, where each spatial unit corresponds to a node. The adjacency relationships are defined based on geographic proximity, using a k-nearest neighbor (KNN) graph, forming a graph that encodes spatial continuity.

(4) Spatial feature learning using GAT

A Graph Attention Network (GAT) was applied to learn spatial dependencies. For a node i with feature vector h_i, the unnormalized attention coefficient with its neighbor j is defined as:

$$e_{ij} = LeakyReLU(a^T[Wh_i \| Wh_j]) \tag{6}$$

where W is a learnable weight matrix, a is the attention vector, and $\|$ denotes concatenation. The normalized attention coefficient is computed via a softmax function over the neighborhood $N_{i:}$

$$\alpha_{ij} = \frac{\exp\left(e_{ij}\right)}{\sum_{k \in N_i} \exp(e_{ik})} \tag{7}$$

where α_{ij} represents the normalized attention weight indicating the importance of node j to node i. The node features are updated as:

$$h'_i = \sigma \sum_{j \in N_i} \left(\alpha_{ij} W h_j\right) \tag{8}$$

By adaptively learning attention weights over neighboring nodes, GAT captures spatially heterogeneous dependencies within local graph structures, thereby improving feature representation in coastal water environments. Multi-head attention is employed to further enhance model stability and representation capacity, enabling the model to capture heterogeneous spatial dependencies in coastal environments.

(5) Model training and experiment configuration

The applicability and effectiveness of the proposed STGNN-TSS model for remote sensing-based TSS retrieval were evaluated through a series of training and comparative experiments using the constructed multitemporal remote sensing dataset.

The study area was first divided into spatial blocks, and these blocks were assigned to the training (70%), validation (20%), and testing (10%) subsets. All temporal observations from sampling nodes within the same block were exclusively assigned to the corresponding subset. Therefore, observations from the same location at different months were not distributed across different subsets, thereby reducing potential spatial and temporal leakage caused by spatial autocorrelation.

For spatial feature learning, a Graph Attention Network (GAT) with a hidden dimension of 64 and two attention heads was adopted. The ELU activation function and a dropout rate of 0.3 were applied to improve model generalization and reduce overfitting. Temporal dependencies were modeled using a single-layer Long Short-Term Memory (LSTM) network with a hidden dimension of 32, followed by a fully connected layer to generate the final TSS predictions.

Model optimization was performed using the Adam optimizer with an initial learning rate of 0.005. The mean squared error (MSE) was used as the loss function, and the model was trained for 500 epochs.

(6) All experiments were implemented using PyTorch (version 2.5.1) and PyTorch Geometric (version 2.6.1) and conducted on an NVIDIA GeForce RTX 3060 Laptop GPU with CUDA 11.8.Comparative experiments and evaluation metrics

To evaluate the performance of the proposed STGNN-TSS model, comparative experiments were conducted against five representative baseline models, including Random Forest (RF), Support Vector Regression (SVR), Multilayer Perceptron (MLP), the Spatiotemporal Graph Convolutional Network (STGCN), and the Adaptive Spatiotemporal Graph Convolutional Network (ASTGCN).

All models were trained and evaluated using the same dataset, data partitioning strategy, and evaluation protocol. Hyperparameters were optimized through grid search or cross-validation to ensure a fair comparison.

Model performance was assessed using three widely adopted regression metrics: the coefficient of determination (R^2), root mean square error (RMSE), and mean absolute error (MAE). These metrics collectively quantify the agreement between the predicted and reference TSS values. Their mathematical formulations are given as follows:

$$R^2 = 1 - \frac{\sum_{i=1}^{n}(y_i - y_i)^2}{\sum_{i=1}^{n}(y_i - y)^2} \tag{9}$$

$$\mathrm{RMSE} = \sqrt{\frac{1}{n}\sum_{i=1}^{n}(y_i - y_i)^2} \tag{10}$$

$$MAE = \frac{1}{n}\sum_{i=1}^{n}|y_i - y_i| \tag{11}$$

where y_i and $\hat{y}_i$ denote the observed and predicted TSS values, respectively, $\bar{y}$ represents the mean of the observed samples, and n is the total number of samples. Higher R^2 values and lower RMSE and MAE values indicate better model prediction performance.

In addition to the conventional regression metrics, the Spearman rank correlation coefficient (Spearman ρ) was employed to evaluate the spatial consistency between STGNN-TSS and independent suspended particulate matter products. Unlike error-based metrics, Spearman correlation measures the monotonic agreement between two datasets based on their ranked values, providing an effective assessment of whether the spatial variation patterns are consistently represented. The coefficient is calculated as follows:

$$\rho = 1 - \frac{6\sum_{i=1}^{n} d_i^2}{n(n^2 - 1)} \tag{12}$$

where d_i represents the difference between the ranks of the STGNN-TSS and reference product values at the i-th spatial location, and n denotes the total number of matched samples. The value of ρ ranges from −1 to 1, with values closer to 1 indicating stronger spatial consistency between the two products.

3. Results

3.1. Model Performance

3.1.1. Overall Model Performance

To comprehensively evaluate the predictive performance and temporal generalization capability of the proposed STGNN-TSS model across representative months, comparative experiments are conducted using three representative monthly datasets (July, October, and December). The proposed STGNN-TSS model is compared with three conventional machine learning models, including Support Vector Regression (SVR), Random Forest (RF), and Multilayer Perceptron (MLP), as well as two advanced spatiotemporal deep learning models, namely the Spatiotemporal Graph Convolutional Network (STGCN) and the Adaptive Spatiotemporal Graph Convolutional Network (ASTGCN). The corresponding results are shown in Figures 3–5, and model performance is quantitatively evaluated using three metrics: R^2, RMSE, and MAE.

The experimental results demonstrate that the proposed STGNN-TSS model consistently achieves superior predictive performance across all three testing scenarios, including two seasonally contrasting months and one transitional month. Among all comparative models, STGNN-TSS achieves the highest R^2 values together with the lowest RMSE and MAE values. Compared with the conventional machine learning models (RF, SVR, and MLP), the proposed model exhibits substantially higher predictive accuracy, indicating that the integration of spatial and temporal information significantly enhances TSS retrieval performance.

Compared with the advanced spatiotemporal deep learning models, STGCN and ASTGCN, the proposed STGNN-TSS model continues to achieve superior performance, further demonstrating the effectiveness of jointly learning spatial dependencies and temporal dynamics. These results confirm that the proposed framework provides a more effective representation of the complex spatiotemporal characteristics of coastal suspended sediments, leading to more accurate and robust large-scale TSS estimation.

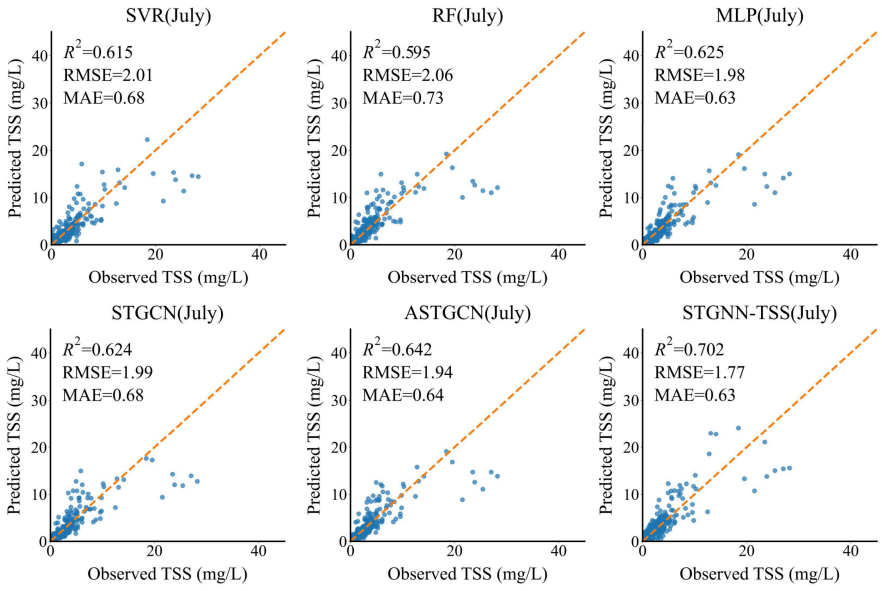


Figure 3. Model performance comparison for July test.

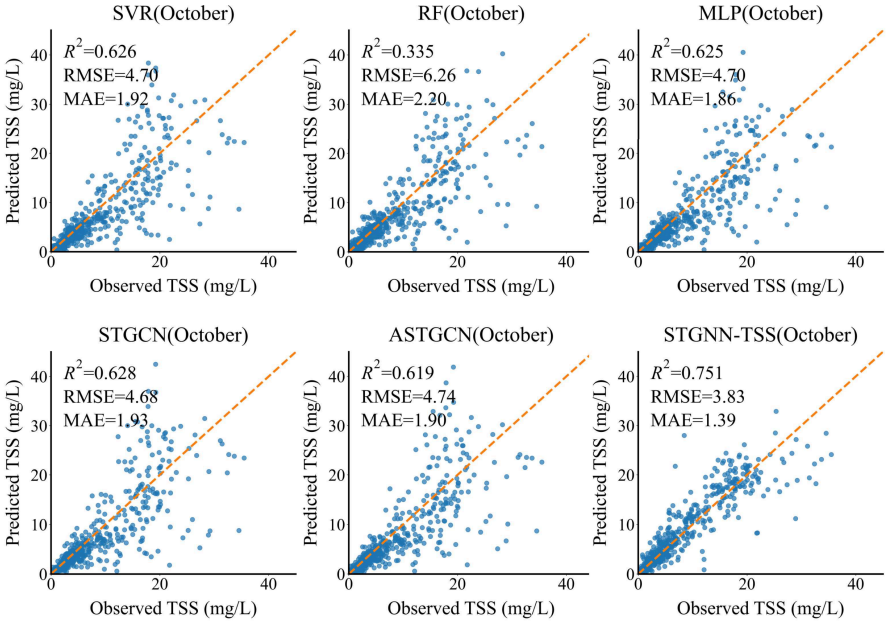


Figure 4. Model performance comparison for October test.

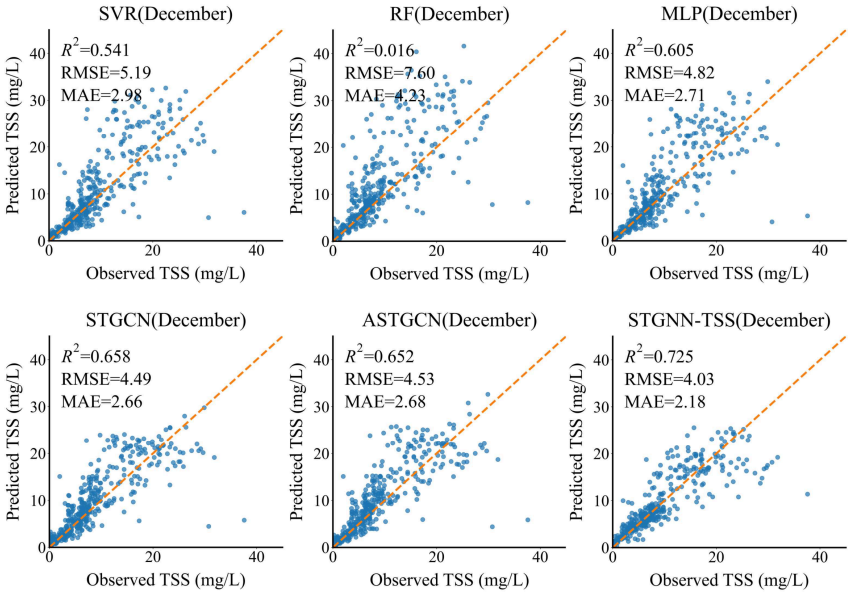


Figure 5. Model performance comparison for December test.

3.1.2. Ablation Analysis of STGNN-TSS Components

A systematic ablation study is conducted to quantify the contribution of each component in the proposed STGNN-TSS framework. All experiments are performed under identical settings, including the same data partitioning strategy, input features, and training epochs, ensuring a fair comparison among different model variants. Four model configurations are evaluated: GAT-MLP, which performs spatial feature learning only; LSTM-MLP, which focuses exclusively on temporal dependency modeling; GAT-LSTM-Linear, which combines spatial and temporal representations using a linear prediction layer; and the complete STGNN-TSS model. Model performance is evaluated using the coefficient of determination (R^2), root mean square error (RMSE), and mean absolute error (MAE). The corresponding results are presented in Figure 6 and Table 1.

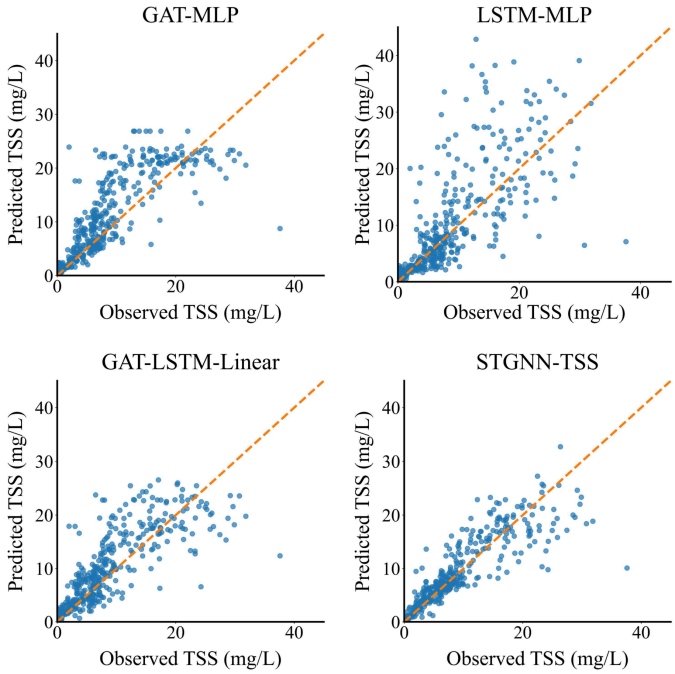


Figure 6. Ablation study of STGNN-TSS.

Table 1. Ablation study of STGNN-TSS.

Model	Description	R^2	RMSE (mg/L)	MAE (mg/L)
GAT-MLP	Without temporal modeling	0.526	5.292	3.309
LSTM-MLP	Without spatial graph attention	0.206	6.847	3.773
GAT-LSTM-Linear	Without the nonlinear MLP prediction head	0.726	4.019	2.059
STGNN-TSS	Full model	0.739	3.924	1.907

As summarized in Table 1, the complete STGNN-TSS model achieves the best overall performance among all model variants, demonstrating the effectiveness of jointly learning spatial dependencies and temporal dynamics. Compared with GAT-MLP, the LSTM-MLP model exhibits lower predictive performance, indicating that temporal features alone are less informative than spatial features in this experiment. Both single-component models perform worse than models combining spatial and temporal information.

The comparison between GAT-LSTM-Linear and STGNN-TSS further highlights the contribution of the nonlinear prediction module. Although GAT-LSTM-Linear benefits from the joint representation of spatial and temporal information, its performance remains slightly lower than that of STGNN-TSS. This result indicates that the nonlinear prediction layer enhances the mapping between multispectral observations and TSS concentrations, thereby improving the representation of complex nonlinear relationships.

Furthermore, both GAT-MLP and LSTM-MLP consistently perform worse than the hybrid models that jointly exploit spatial and temporal information, confirming the complementary roles of spatial and temporal feature learning in TSS retrieval. The consistent improvements achieved by STGNN-TSS across all evaluation metrics demonstrate that the proposed framework effectively captures both spatial heterogeneity and temporal dynamics, leading to more accurate and robust large-scale coastal TSS estimation.

3.1.3. Temporal Prediction Performance and Dynamic Response Characteristics

To evaluate the temporal fitting performance and dynamic response capability of the proposed STGNN-TSS model, two representative coastal sites are selected: one located in Bohai Bay (Figure 7a) and the other along the southern Fujian coast (Figure 7b). These sites represent contrasting hydrodynamic and sedimentary environments in northern and southern China. At each site, the reference and predicted TSS time series produced by both the STGNN-TSS and RF models are compared, with fitted trend lines included to illustrate temporal variation over the comparison period.

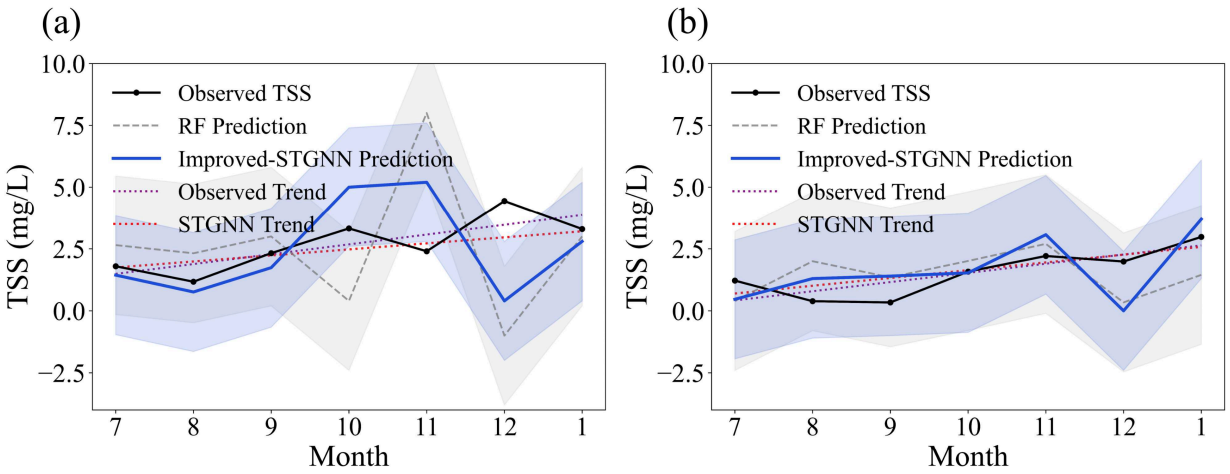


Figure 7. Comparison of observed and predicted TSS time series at representative coastal sites, with blue and gray shaded areas indicating the ±RMSE ranges for the Improved-STGNN and RF models, respectively. (**a**) Bohai Bay station; (**b**) southern Fujian coastal station.

At both sites, the STGNN-TSS predictions broadly followed the temporal variation in the reference series, although discrepancies remained in individual months. Minor discrepancies are observed in December for both models, which are likely associated with localized uncertainties in the remote sensing data. Nevertheless, the STGNN-TSS model exhibits lower sensitivity to these disturbances than the RF model, indicating stronger temporal stability and greater robustness to observational noise.

3.1.4. Spatial Generalization Performance

The spatial generalization capability of the proposed STGNN-TSS model is evaluated by dividing China's coastal waters into three latitudinal zones (Lat > 36°, 29° ≤ Lat ≤ 36°, and Lat < 29°). Within each zone, the predicted TSS values are compared with the corresponding reference values (Figure 8a–c). The model consistently achieves strong predictive performance across all three regions, with R^2 ranging from 0.827 to 0.909 and RMSE varying between 1.58 and 2.61 mg L^{-1}. These results demonstrate the ability of the proposed model to capture spatial variability under diverse environmental conditions.

To further evaluate the model performance across different coastal environments, the study area was divided into inshore and offshore waters (Figure 9). Sampling points were categorized into two groups representing regions with different levels of coastal sediment influence. In inshore waters, the model achieved an R^2 of 0.869 and an RMSE of 2.425 mg L^{-1}. In offshore waters, the model achieved an R^2 of 0.678 and an RMSE of 0.772 mg L^{-1}. The relatively lower R^2 in offshore waters is associated with the low TSS concentration range and limited variability typically observed in clearer waters. In these regions, many observations are close to 0–1 mg L^{-1}, and the small variance of reference values makes R^2 more sensitive to small absolute deviations between predictions and observations. A small number of

low-concentration pixels may also exhibit slight deviations due to uncertainties in satellite observations and model prediction under near-zero concentration conditions, which can further influence statistical metrics.

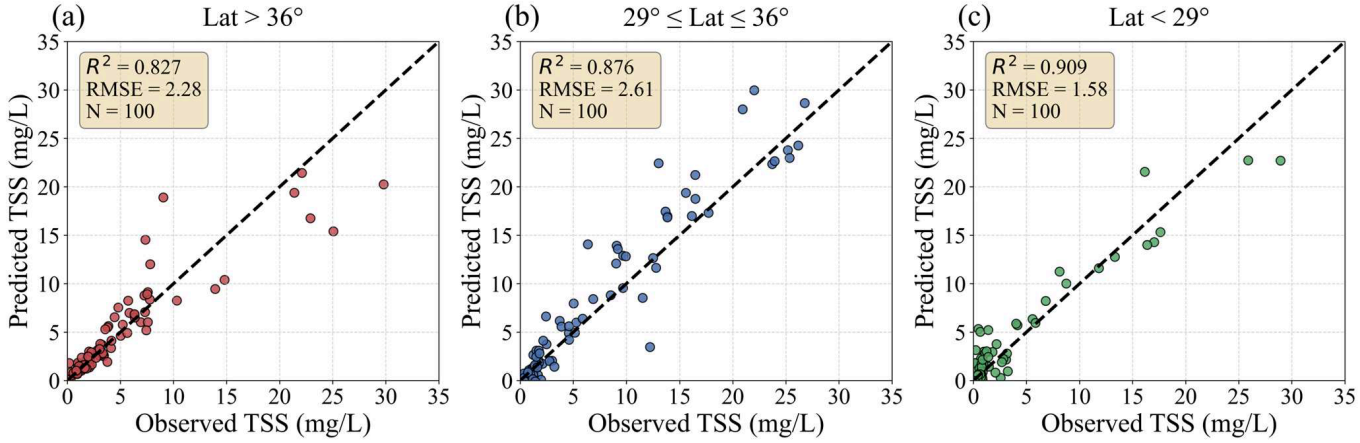


Figure 8. Comparison of observed and predicted TSS across different latitude zones: (**a**) Lat > 36°, (**b**) 29° ≤ Lat ≤ 36°, (**c**) Lat < 29°. The inset shows R^2, RMSE, and sample size (N) for each zone.

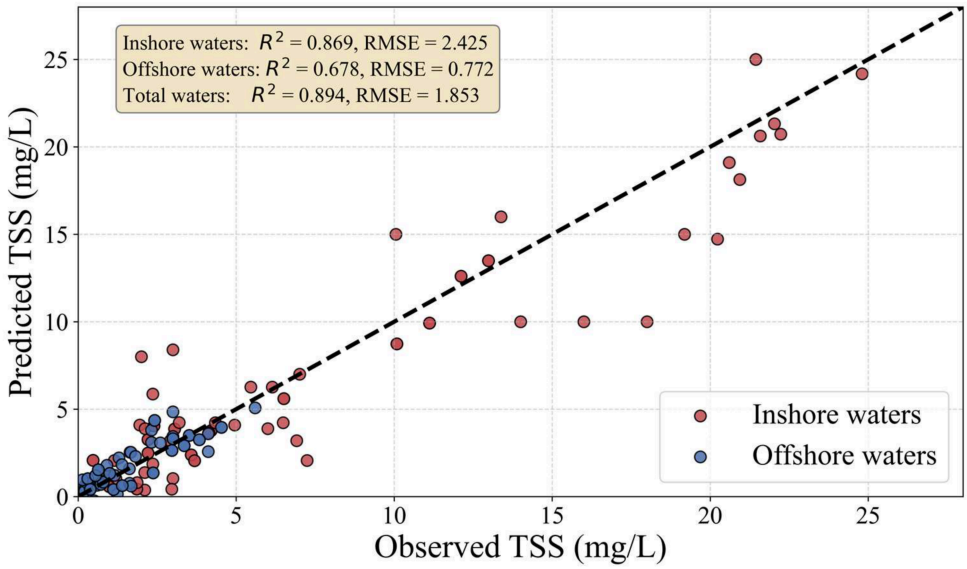


Figure 9. Comparison of observed and predicted TSS in inshore waters and offshore waters. Insets show R^2 and RMSE for inshore waters, offshore waters, and the total dataset.

When all samples are considered together, the proposed model achieves an overall R^2 of 0.894 and an RMSE of 1.853 mg L^{-1}, demonstrating its ability to capture TSS variations across heterogeneous coastal environments.

3.1.5. Interpretation of Spectral Contributions in STGNN-TSS Using SHAP Analysis

SHAP analysis was conducted to quantify the contribution of Sentinel-2 spectral bands to TSS estimation and to characterize the spectral information utilized by the STGNN-TSS model. October was selected as the representative period because of its relatively stable seasonal conditions and sufficient valid observations. The SHAP values of each spectral band were calculated to evaluate its relative contribution to the model predictions.

The results demonstrate that STGNN-TSS relies on the combined information from multiple spectral bands rather than a single spectral feature (Figure 10a). Among all input bands, B4 (red), B2 (blue), and B5 (red-edge) exhibited larger SHAP values, indicating their

greater influence on TSS estimation. These bands are closely related to the optical response of suspended materials in coastal waters and provide important spectral information for distinguishing TSS variations. The near-infrared and shortwave infrared bands showed relatively lower contributions but remained complementary to the prediction process.

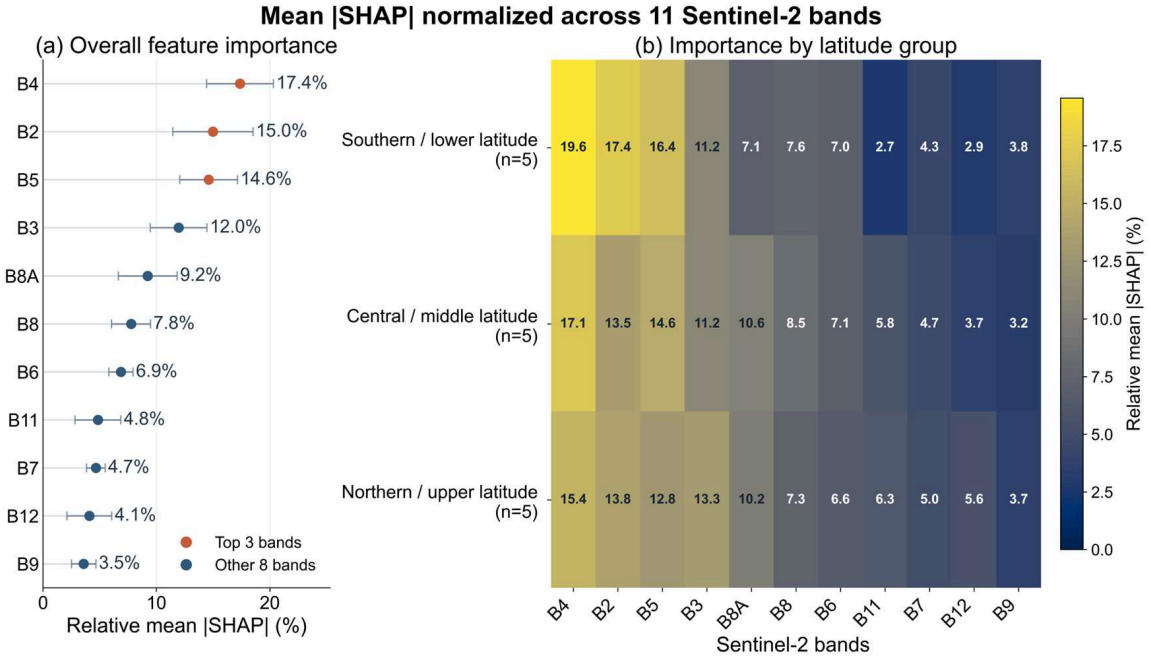


Figure 10. Spectral contribution analysis of Sentinel-2 bands in STGNN-TSS based on SHAP values. (**a**) Overall contribution of Sentinel-2 spectral bands; (**b**) regional variations in spectral contributions across different coastal zones.

The spatial variability of spectral contributions was further examined using latitude-based SHAP analysis, with the coastal zone divided into three regions (Lat $> 36°$, $29° \leq$ Lat $\leq 36°$, and Lat $< 29°$) (Figure 10b). The contribution patterns of Sentinel-2 bands differed among the three regions. Northern, central, and southern coastal waters showed distinct spectral importance characteristics, reflecting differences in regional optical conditions. This variation suggests that STGNN-TSS can utilize region-specific spectral information and maintain a flexible spectral response relationship across heterogeneous coastal environments.

3.1.6. Spatial Consistency Assessment with Independent Satellite-Derived Products

The spatial patterns of the reconstructed STGNN-TSS dataset were further compared with two independent satellite-derived suspended particulate matter (SPM) products, including the NOAA VIIRS+OLCI SPM product and the GlobColour SPM-OC5 product. Although total suspended solids (TSS) and suspended particulate matter (SPM) differ in their measurement definitions and retrieval approaches, both parameters characterize the abundance and spatial distribution of suspended materials in aquatic environments, making the external SPM products suitable for evaluating the spatial consistency of the reconstructed TSS dataset.

The NOAA MSL12 multi-sensor SPM product is a global ocean color dataset generated from observations of multiple satellite sensors, including VIIRS onboard the Suomi-NPP and NOAA-20 satellites and the Sentinel-3A OLCI sensor. The product applies the MSL12 ocean color processing system to retrieve suspended particulate matter concentration and further incorporates the Data Interpolating Empirical Orthogonal Function (DINEOF) method to reconstruct spatial gaps caused by missing observations. Consequently, the

product provides spatially continuous SPM estimates at an approximate spatial resolution of 2 km [44].

In this study, daily NOAA MSL12 SPM observations were aggregated into monthly composites to match the temporal resolution of the STGNN-TSS dataset. Monthly SPM values were calculated from valid daily observations after quality control, and pixels with insufficient observations were excluded. The resulting monthly NOAA SPM products were subsequently reprojected to the geographic coordinate system of the STGNN-TSS dataset.

The GlobColour SPM-OC5 product is a Level-3 ocean color composite dataset generated by the ACRI-ST GlobColour project and distributed through the Copernicus Marine Service. It provides mapped SPM concentrations derived from multi-sensor ocean color observations, including MODIS-Aqua, VIIRS, Sentinel-3A OLCI, NOAA-20 VIIRS, and Sentinel-3B OLCI. The SPM retrieval is based on the OC5 algorithm proposed by Gohin [45], which estimates suspended particulate matter concentrations from ocean reflectance characteristics. The original GlobColour SPM-OC5 product has a spatial resolution of approximately 4 km. Daily observations were aggregated into monthly composites for comparison with STGNN-TSS, and all datasets were transformed into a common geographic coordinate system. Considering the resolution difference between datasets, the 60 m STGNN-TSS maps were aggregated to the spatial resolution of the external products using area-weighted averaging before pixel-wise comparison.

The spatial distributions of the reconstructed STGNN-TSS product, the NMDIS GOCI-derived TSS product, the NOAA VIIRS+OLCI SPM product, and the GlobColour SPM-OC5 product are compared in Figure 11 for January and July 2020. The reconstructed STGNN-TSS product reproduced the major spatial patterns observed in the original NMDIS GOCI-derived TSS product and showed consistent spatial distributions with the independent satellite-derived SPM products.

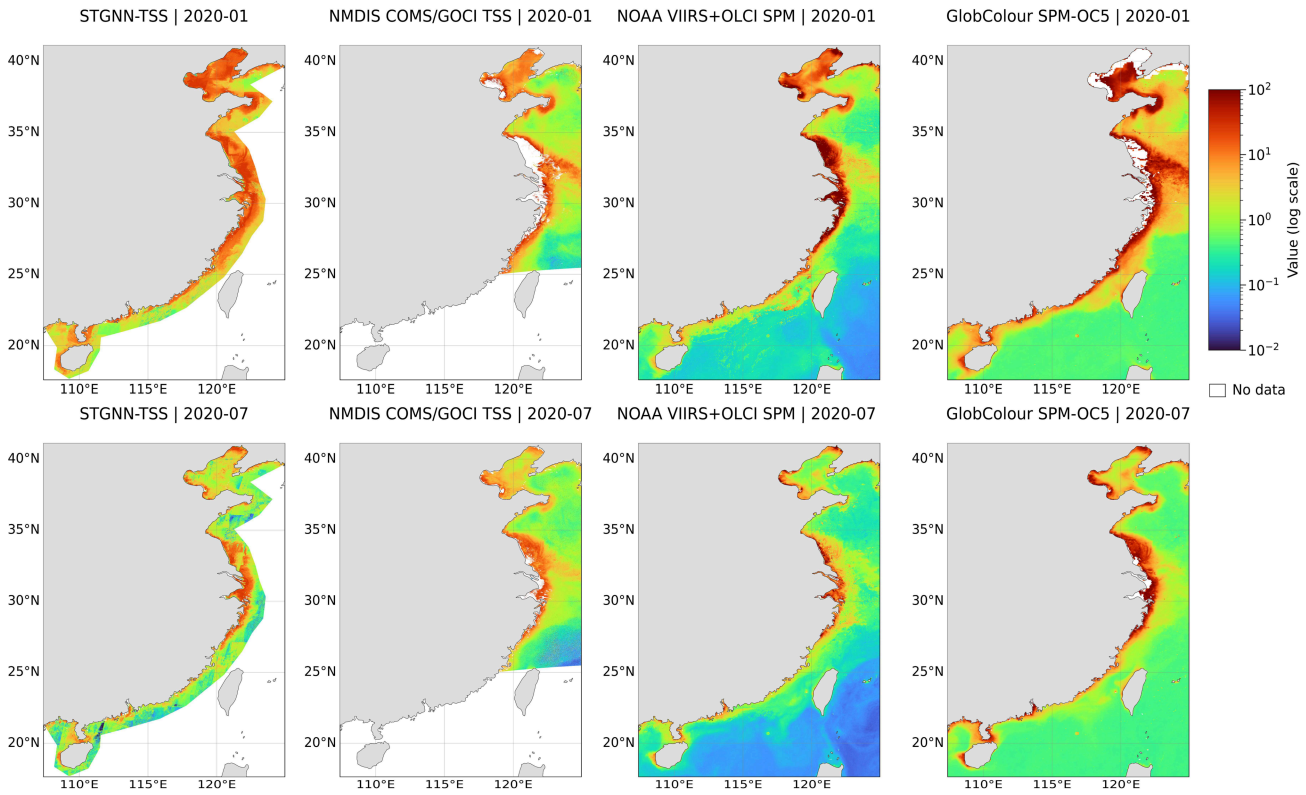


Figure 11. Spatial comparison of the reconstructed STGNN-TSS product with the original GOCI-derived TSS product and independent satellite-derived SPM products in 2020.

Figure 12 presents the seasonal spatial distributions of the reconstructed STGNN-TSS product and the two independent satellite-derived SPM products in winter and summer 2024. High suspended sediment concentrations were consistently observed in the Bohai Sea, the Yangtze River Estuary, and other nearshore regions, whereas offshore waters generally exhibited lower concentrations. Similar spatial gradients were captured by the reconstructed STGNN-TSS product and the independent SPM products, with consistent high-concentration regions identified in major estuaries and coastal zones.

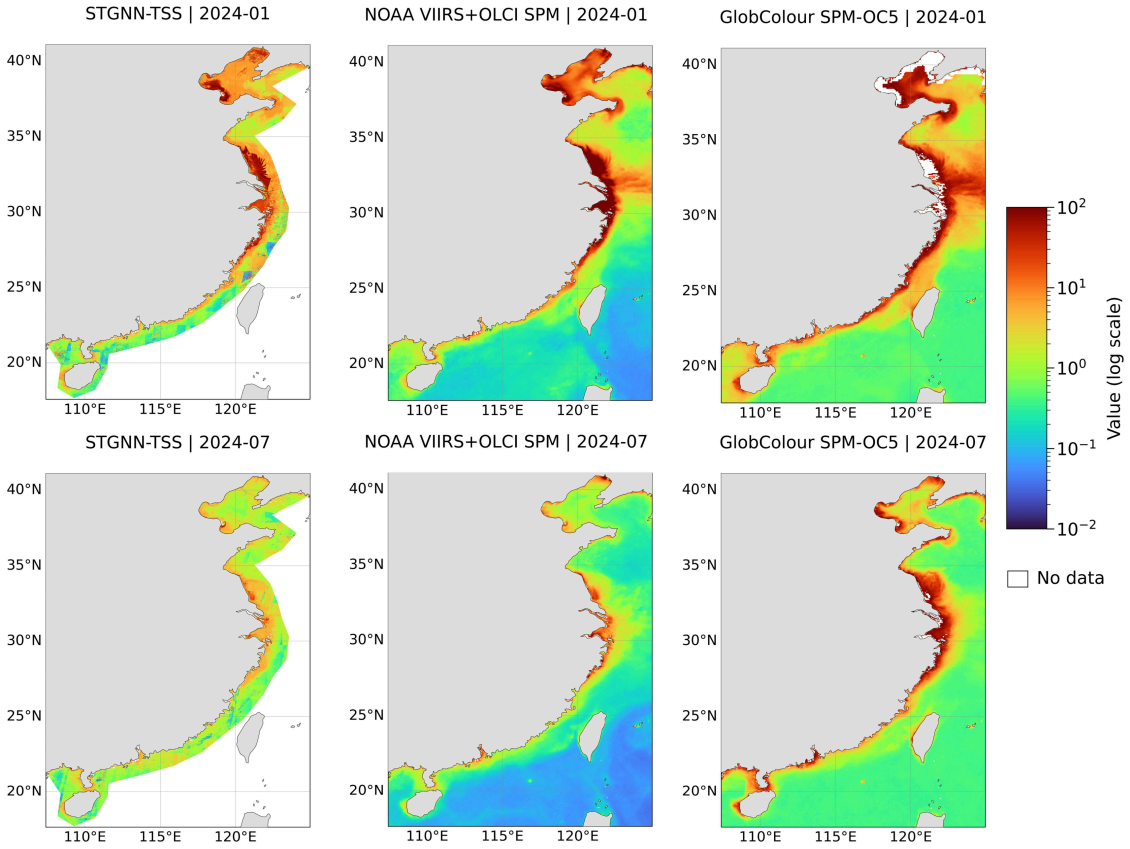


Figure 12. Spatial comparison of the reconstructed STGNN-TSS product and independent satellite-derived SPM products in 2024.

Pixel-wise comparisons were conducted between the reconstructed STGNN-TSS product and two independent SPM products to evaluate their spatial consistency (Figure 13). Given the differences in sensor characteristics, retrieval algorithms, spatial resolutions, and parameter definitions among satellite-derived products, the comparison focused on the consistency of spatial distribution patterns rather than the equivalence of absolute concentration values. The Spearman rank correlation coefficient (ρ) was used to quantify the agreement in spatial variations.

The density scatter plots show positive monotonic relationships between the STGNN-TSS product and both independent SPM products during winter and summer 2024. In January 2024, the STGNN-TSS product showed strong agreement with the NOAA VIIRS+OLCI SPM and GlobColour SPM-OC5 products, with Spearman correlation coefficients of 0.891 and 0.860, respectively. In July 2024, the corresponding ρ values were 0.738 and 0.741. These results indicate that the STGNN-TSS product maintained consistent spatial variation characteristics with independent satellite-derived SPM products under contrasting seasonal conditions.

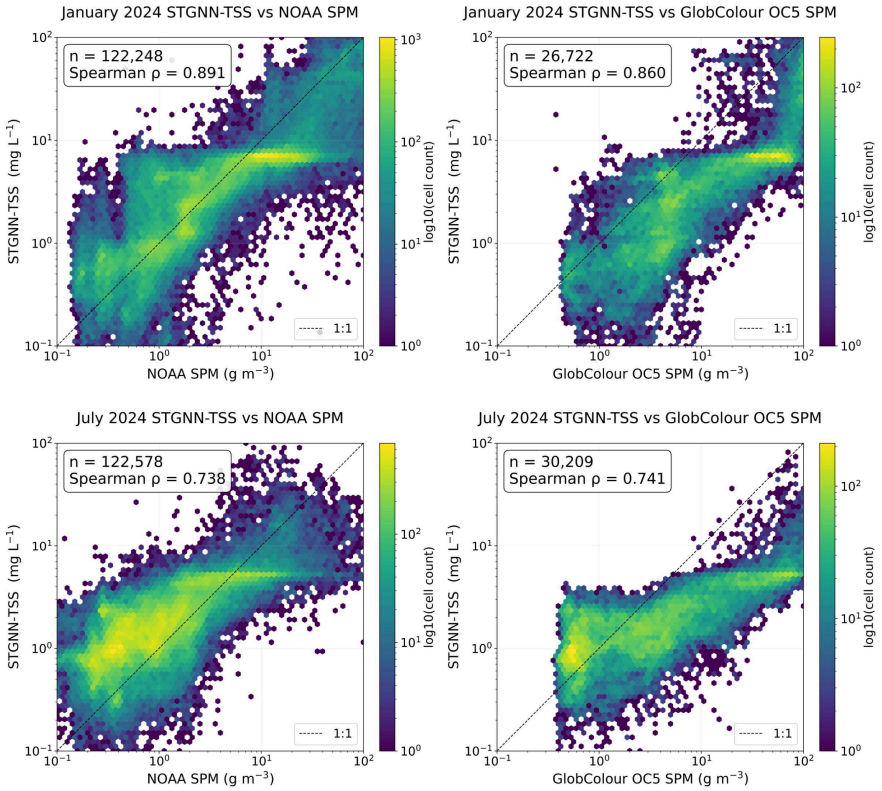


Figure 13. Pixel-wise comparison between the reconstructed STGNN-TSS product and independent satellite-derived SPM products in winter and summer 2024.

3.2. Overall Spatial Distribution Pattern of TSS Along the China Coast

Monthly mean TSS distributions for the period 2016–2025 are reconstructed using the proposed STGNN-TSS model, from which annual mean distribution maps are derived (Figure 14). The reconstructed TSS fields exhibit a pronounced "high-inshore, low-offshore" spatial pattern along the Chinese coast. Elevated TSS concentrations are primarily distributed in estuaries, shallow tidal flats, and semi-enclosed bays, whereas offshore waters remain characterized by relatively low concentrations and high spatial homogeneity. This large-scale spatial pattern reflects the combined influence of hydrodynamic conditions, sediment availability, and terrestrial sediment inputs, resulting in distinct regional gradients in TSS distribution.

To further characterize regional differences, the study area is divided into four representative coastal regions: the Bohai Sea, Yellow Sea, East China Sea, and northern South China Sea (Figure 14). The multi-year mean TSS distributions for these regions are summarized using violin plots (Figure 15). Among the four regions, the Bohai Sea exhibits the highest mean TSS concentration (approximately 1.41 mg L^{-1}) together with the largest variability, indicating pronounced spatial heterogeneity. The Yellow Sea ranks second (approximately 1.20 mg L^{-1}), with elevated concentrations occurring mainly near the Yellow River estuary and along the southern Jiangsu coast. The East China Sea exhibits a lower regional mean (approximately 1.00 mg L^{-1}), with peak TSS concentrations concentrated around the Yangtze River estuary and gradually decreasing toward offshore waters. In contrast, the northern South China Sea exhibits the lowest mean TSS concentration (approximately 0.26 mg L^{-1}), with elevated values largely confined to localized estuarine and nearshore areas.

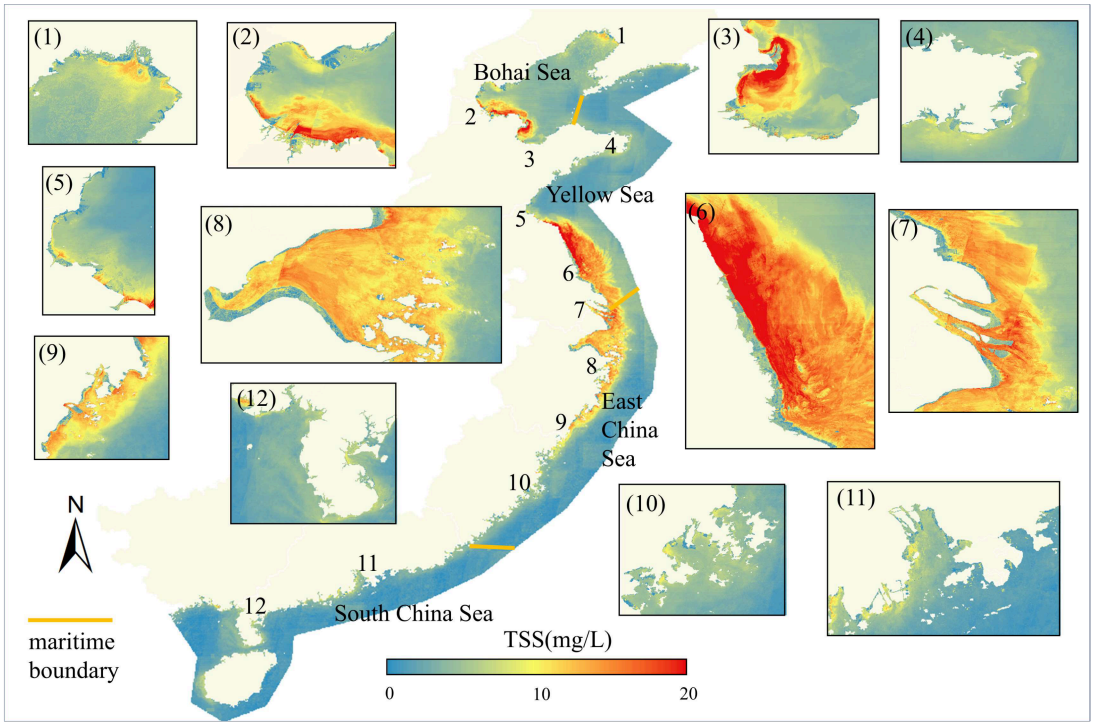


Figure 14. Overall spatial distribution map of TSS along the coast of China. 12 regions from north to south were selected for zooming in to show the detailed distribution of TSS: (1) northern Bohai Sea; (2) western Bohai Sea; (3) southern Bohai Sea; (4) northern Yellow Sea coast; (5) northern Yellow Sea coast; (6) central Yellow Sea coast; (7) southern Yellow Sea coast; (8) northern East China Sea coast; (9) central East China Sea coast; (10) southern East China Sea coast; (11) Pearl River Estuary; and (12) coastal waters of the Guangxi Zhuang Autonomous Region.Yellow lines indicate sea area boundaries according to the "China Sea Area Division Standard".

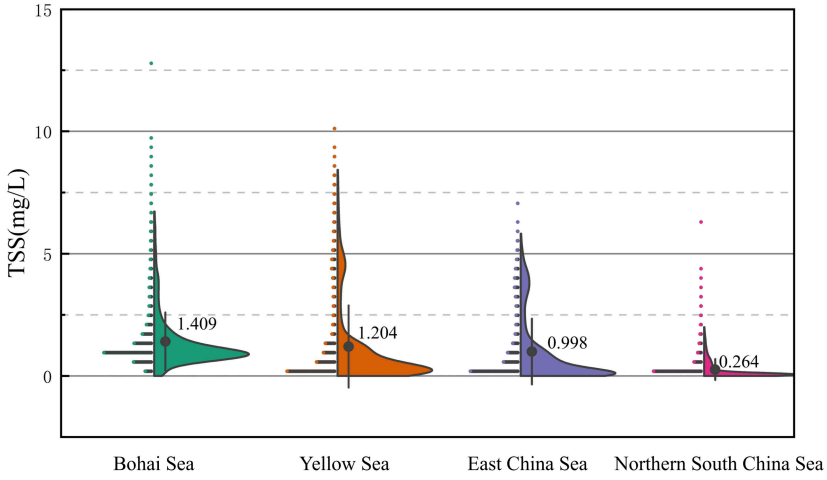


Figure 15. Violin plots of long-term mean total suspended solids (TSS) distributions across four coastal regions of China (Bohai Sea, Yellow Sea, East China Sea, and the northern South China Sea) during 2016–2025.

3.3. Seasonal Variability of TSS in China's Coastal Waters

Monthly TSS retrievals for the period 2016–2025 are averaged to generate multi-year monthly mean distribution maps (Figure 16) and statistical boxplots (Figure 17), providing an overview of the seasonal variability of suspended sediments along the Chinese coast. The reconstructed TSS dataset reveals a pronounced seasonal cycle, characterized by elevated

concentrations in winter, reduced concentrations in summer, and intermediate levels during spring and autumn.

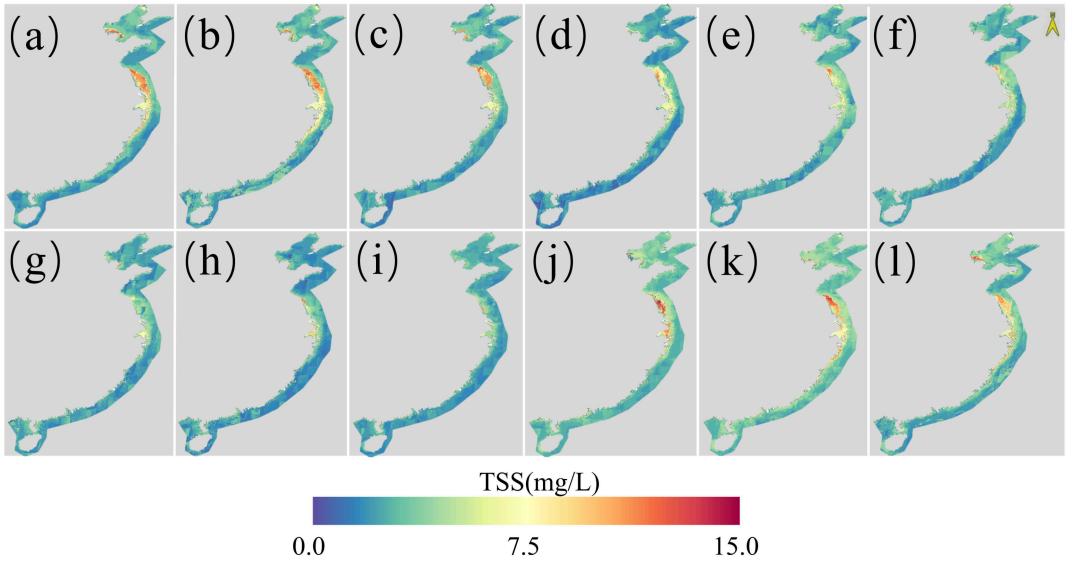


Figure 16. Multi-year mean monthly distributions of TSS along the coast of China ((**a**–**l**): January–December).

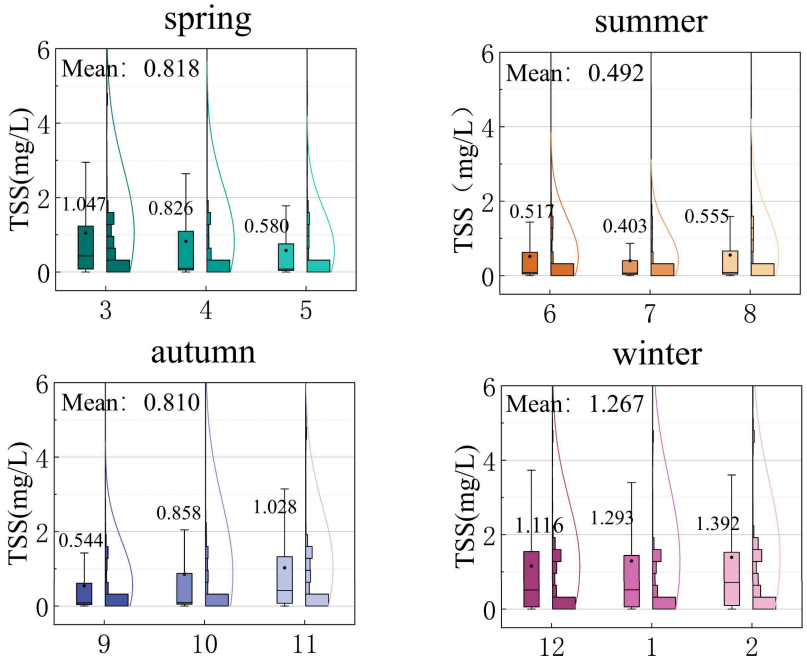


Figure 17. Monthly boxplots of total suspended solids (TSS) along the coast of China based on multi-year (2016–2025) mean statistics. The number next to each box represents the corresponding monthly mean TSS.

During spring, TSS concentrations remain at moderate levels, with high-value regions primarily distributed around major estuaries and shallow tidal flats. Compared with winter, these high-concentration areas contract slightly. In summer, TSS concentrations reach their annual minimum, and elevated values are largely confined to a few localized nearshore regions. During autumn, TSS concentrations increase gradually, with high-concentration zones expanding along the southern Jiangsu coast and around the Yangtze River estuary. In winter, TSS concentrations reach their annual maximum, accompanied

by higher median and mean values, larger upper quartiles, and greater spatial variability, especially in nearshore and shallow-water environments.

The seasonal differences between summer and winter (Figure 18) further illustrate the spatial characteristics of TSS variability. In winter, TSS concentrations increase markedly throughout most nearshore waters, particularly in Bohai Bay, the Yellow River estuary, and along the Jiangsu coast, where continuous high-concentration belts are formed. In contrast, offshore waters exhibit relatively small seasonal changes, with TSS differences remaining close to zero over large areas. Within the Yangtze River estuary, TSS remains relatively stable or decreases slightly in the inner estuary, whereas pronounced increases are observed in the outer estuary and adjacent coastal waters.

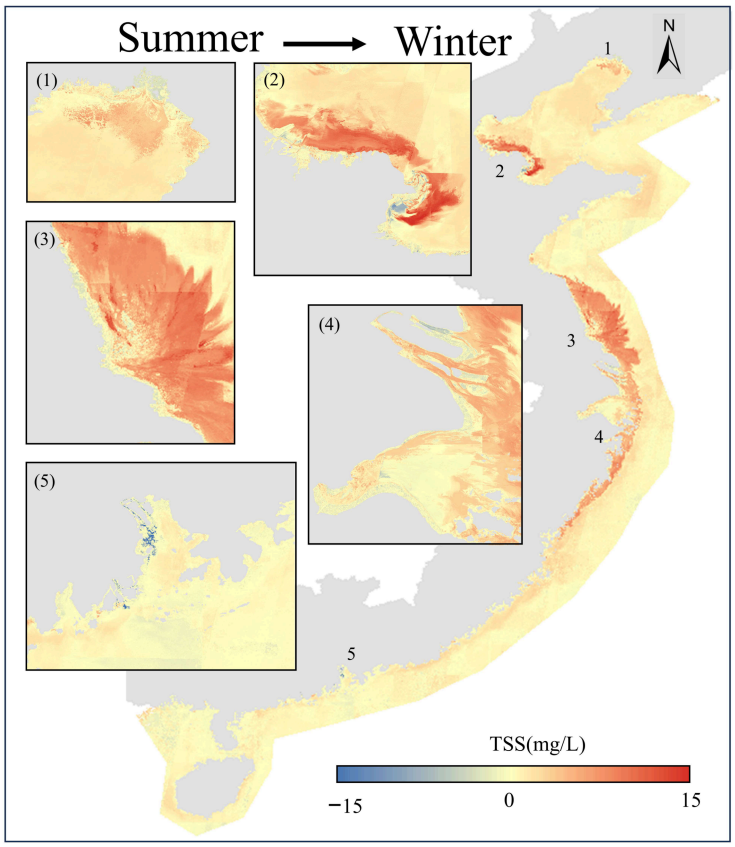


Figure 18. Multi-year average seasonal variation in TSS along the coast of China from summer to winter. Five representative coastal regions were selected from north to south to illustrate the detailed spatial variations: (1) northern Bohai Sea; (2) southern Bohai Sea; (3) Jiangsu coastal waters; (4) Yangtze River Estuary; and (5) Pearl River Estuary.

The Pearl River estuary and its adjacent waters (Figure 18(5)) exhibit a distinctly different seasonal pattern. TSS variability within the core estuarine region remains relatively weak, while localized areas exhibit higher concentrations during summer owing to enhanced river runoff. This pattern reflects the dominant influence of riverine sediment discharge. During the summer flood season, abundant sediment inputs, together with freshwater plume expansion and water-column stratification, maintain relatively high surface TSS concentrations. In winter, reduced river discharge substantially limits sediment supply, and wind-wave-induced resuspension alone is insufficient to sustain similarly high TSS levels.

Overall, the seasonal variability of TSS exhibits pronounced regional differences that are generally consistent with previous studies [46–49]. Although most coastal regions follow a typical winter-high, summer-low pattern, regional deviations occur because of the

combined influences of riverine sediment input, seabed characteristics, water depth, and monsoon-driven hydrodynamic processes.

3.4. Interannual Variability and Long-Term Trends

3.4.1. Interannual Variability of TSS Along the Coast of China

Based on reconstructed monthly TSS data during 2016–2025, interannual variability and long-term evolution of suspended sediments along the Chinese coast are analyzed (Figure 19). To better characterize temporal changes, the study period is divided into two phases: 2016–2020 and 2020–2025.

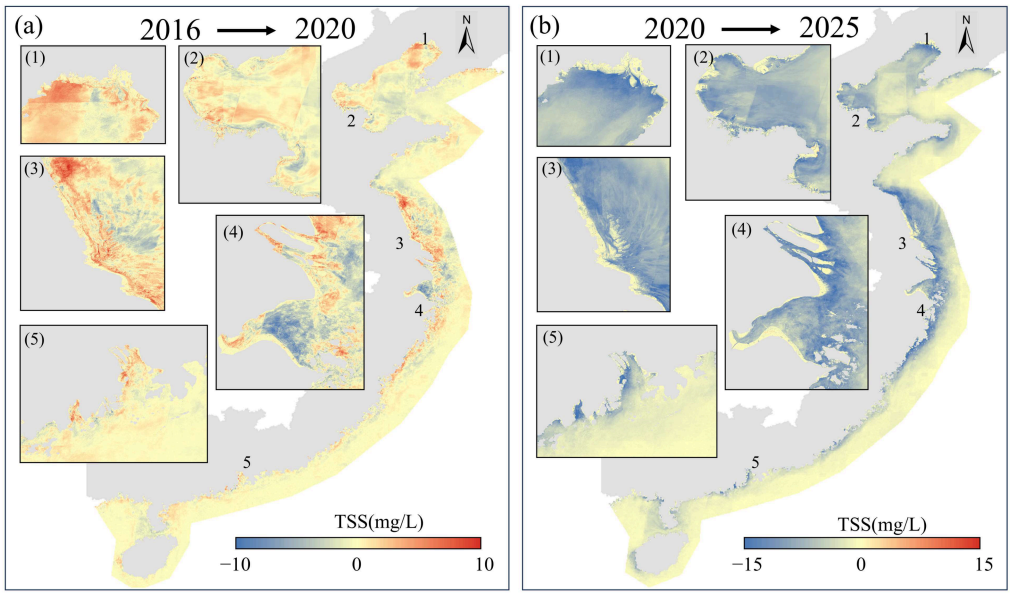


Figure 19. Interannual variation patterns of TSS along the coast of China: (**a**) 2016–2020 and (**b**) 2020–2025. Five representative coastal regions were selected from north to south to illustrate the detailed spatial variations: (1) northern Bohai Sea; (2) southern Bohai Sea; (3) Jiangsu coastal waters; (4) Yangtze River Estuary; and (5) Pearl River Estuary.

During 2016–2020, TSS concentrations in the nearshore waters of northern China generally exhibit an increasing trend (Figure 19a), particularly in Laizhou Bay, the Yellow River Estuary, and the shallow coastal waters of Jiangsu Province. These regions, characterized by shallow bathymetry and abundant fine-grained sediments, are highly responsive to hydrodynamic forcing and sediment resuspension. In the Yangtze River estuary, TSS exhibits pronounced interannual variability with a slight increasing trend, whereas the adjacent offshore waters display a fan-shaped pattern of decreasing TSS extending seaward.

During 2020–2025 (Figure 19b), TSS concentrations generally exhibit a decreasing trend along most sections of the Chinese coast, with the most pronounced reductions occurring near major estuaries. Meanwhile, the regions exhibiting strong interannual variability gradually expand from the northern shallow seas toward the mid-latitude coastal zone, indicating increasing regional differences in sediment dynamics.

3.4.2. Long-Term TSS Time Series at Representative Bays and Estuaries

To investigate long-term variability under different hydrodynamic conditions, five representative coastal regions are selected: Laizhou Bay, the eastern Jiangsu coast, the Yangtze River estuary, Ningde Bay, and the Pearl River estuary (Figure 1). These regions represent a range of coastal environments, including semi-enclosed shallow seas, muddy

tidal flats, river-dominated estuaries, and subtropical coastal waters. Monthly TSS time series for the period 2016–2025 are reconstructed for each region (Figure 20).

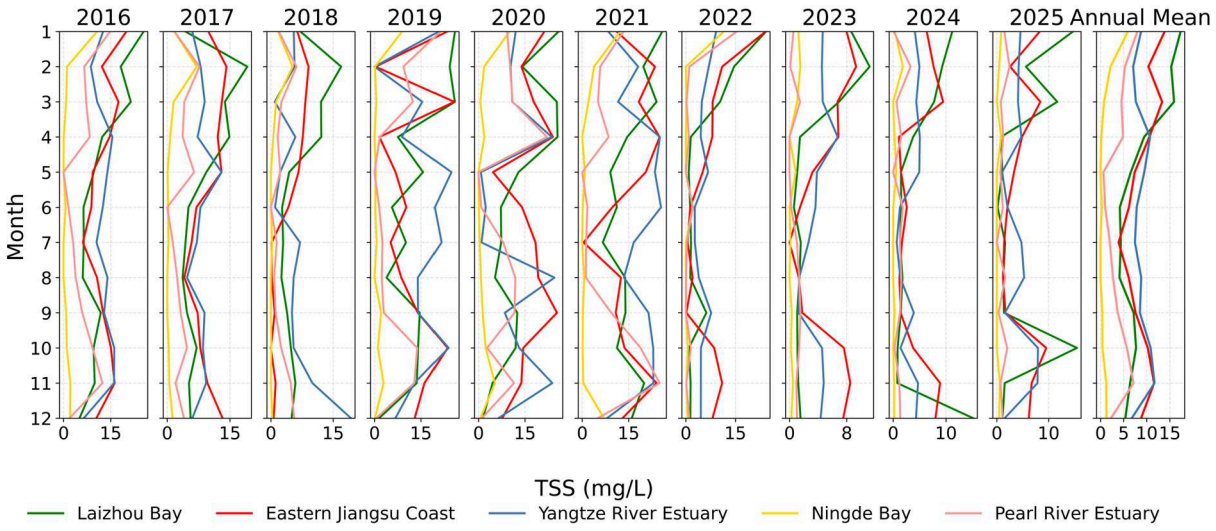


Figure 20. Long-term monthly TSS time series at five representative coastal and estuarine sites along the Chinese coast during 2016–2025.

Laizhou Bay exhibits the largest temporal variability, characterized by pronounced seasonal fluctuations and substantial interannual differences, reflecting its shallow bathymetry and abundant fine-grained sediments. The eastern Jiangsu coast exhibits comparatively stable temporal variations with distinct seasonal cycles and persistent wet–dry seasonal contrasts. The Yangtze River estuary displays more complex temporal behavior, driven by the combined influences of river discharge, tidal processes, extreme weather events, and human activities. Ningde Bay maintains relatively low TSS concentrations and limited temporal variability because of its deeper water, coarser seabed sediments, and relatively weak terrestrial sediment inputs, although occasional short-term increases are associated with typhoon events and intense precipitation. The Pearl River estuary consistently exhibits low and relatively stable TSS concentrations, reflecting limited sediment supply and comparatively clear coastal waters.

4. Discussion

4.1. Physical and Environmental Drivers of TSS Variability

The spatiotemporal variability of total suspended solids (TSS) along the Chinese coast reflects the combined influence of hydrodynamic forcing, sediment characteristics, terrestrial sediment inputs, and anthropogenic activities operating across multiple spatial and temporal scales. The reconstructed TSS dataset reveals a persistent "high-inshore, low-offshore" spatial pattern, pronounced seasonal variability, and distinct interannual evolution, collectively highlighting the dominant role of coupled physical and environmental processes in regulating suspended sediment dynamics.

At the spatial scale, TSS distribution is primarily controlled by water depth, sediment properties, and local hydrodynamic conditions. Shallow nearshore waters characterized by fine-grained sediments exhibit relatively low critical shear stress for sediment resuspension and are therefore highly sensitive to wind, wave, and tidal forcing, resulting in persistently elevated and spatially heterogeneous TSS concentrations. In contrast, deeper offshore waters with coarser seabed sediments experience weaker resuspension and reduced terrestrial influence, leading to comparatively low and stable TSS concentrations. Regional differences further reflect distinct dominant forcing mechanisms. Northern shallow seas, including

Bohai Bay and the Jiangsu coast, are mainly influenced by wind-wave-induced sediment resuspension, whereas the Yangtze River estuary is primarily controlled by the interaction between river discharge and tidal mixing. In contrast, the southern coastal region is more strongly affected by seasonal precipitation, typhoon activity, and coastal circulation.

At the seasonal scale, TSS variability exhibits pronounced regional differences. In northern coastal waters, seasonal fluctuations are dominated by the East Asian winter monsoon, which enhances wind-wave resuspension during winter and produces a characteristic winter-high, summer-low pattern. In contrast, seasonal variability in southern estuarine and coastal waters is more strongly regulated by river discharge, with increased sediment inputs during the wet season and comparatively stable conditions during the dry season.

At the interannual scale, the transition from increasing TSS during 2016–2020 to a generally decreasing trend during 2020–2025 suggests the combined influence of changing sediment supply, hydrodynamic conditions, and human activities. Although the relative contributions of these factors are not explicitly quantified in this study, the coherent spatial patterns indicate that large-scale environmental regulation, river basin management, and coastal engineering projects may have contributed to the observed long-term evolution.

Beyond natural forcing, anthropogenic activities further modify suspended sediment dynamics. River regulation, sediment retention by reservoirs, port construction, land reclamation, and ecological restoration projects alter sediment supply, hydrodynamic conditions, and sediment transport pathways. The interaction between natural and human-induced processes enhances regional heterogeneity, resulting in highly dynamic TSS conditions in nearshore waters while maintaining comparatively stable conditions in offshore regions.

4.2. Applicability and Limitations for Large-Scale TSS Retrieval

Accurate retrieval of TSS over large spatial and temporal domains requires models capable of simultaneously representing spatial heterogeneity and temporal dynamics. Conventional machine learning approaches based on pixel-wise assumptions or empirical relationships often exhibit limited transferability across regions and time, making it difficult to generate spatially and temporally consistent long-term TSS products.

The proposed STGNN-TSS framework addresses this limitation by jointly learning spatial dependencies and temporal dynamics from multitemporal satellite observations. The consistently high prediction accuracy achieved across different coastal regions, together with the coherent spatial distribution and temporal evolution of the reconstructed TSS dataset, demonstrates the effectiveness of the proposed framework for large-scale coastal TSS retrieval. More importantly, the capability to reconstruct continuous monthly TSS products over a ten-year period provides valuable support for long-term coastal environmental monitoring and change analysis.

Nevertheless, several limitations remain. First, spatial relationships are represented using a static graph structure based on spatial proximity and therefore do not explicitly incorporate dynamic hydrodynamic processes, such as tidal currents, residual circulation, or sediment transport pathways. Second, temporal variations in image quality and data availability may affect local prediction accuracy, particularly in regions frequently affected by cloud contamination. Finally, although the proposed framework effectively captures spatiotemporal patterns in TSS, it remains a data-driven model and does not explicitly resolve the underlying physical mechanisms governing sediment transport.

Future research will focus on integrating physical process information, such as hydrodynamic simulations and environmental forcing variables, into the graph learning framework to further improve model interpretability and prediction accuracy.

4.3. Uncertainty and Limitations

Despite the encouraging performance of the proposed framework, uncertainties remain in large-scale, long-term TSS reconstruction. These uncertainties primarily originate from satellite observations, data processing procedures, and the inherent complexity of coastal environments. Although the reconstructed dataset captures the major spatial patterns and long-term variability characteristics supported by internal evaluation and comparisons with independent satellite-derived products, uncertainty inevitably increases when interpreting localized or short-term variations. Performance is limited at high TSS concentrations, and estimates in this range should be interpreted cautiously.

Satellite image quality is affected by cloud contamination, atmospheric correction, observation geometry, and sensor noise, all of which introduce spatiotemporal inconsistencies into the input data. These effects are particularly evident in low-latitude regions where cloud cover is persistent. In addition, large-scale image processing procedures, including image tiling and mosaicking, may introduce minor discontinuities in regions with strong spatial gradients, although their influence on long-term average TSS distributions is generally limited.

Environmental variability also contributes to retrieval uncertainty. Episodic events, such as typhoons, storm surges, extreme river discharge, and short-term sediment resuspension, may not be fully represented by monthly composite products or multi-year averages. Consequently, the reconstructed dataset is more suitable for investigating regional-scale spatial patterns and long-term temporal evolution than for interpreting individual short-term events.

5. Conclusions

This study proposes a Spatiotemporal Graph Neural Network for Total Suspended Solids (STGNN-TSS) by integrating graph attention networks with temporal sequence modeling. Using Sentinel-2 imagery, the proposed framework reconstructs monthly TSS dynamics in China's coastal waters during 2016–2025. The main conclusions are summarized as follows.

(1) Model performance and capability.

The proposed STGNN-TSS framework effectively captures both spatial dependencies and temporal dynamics of TSS, supporting TSS retrieval across heterogeneous coastal environments. By jointly learning graph-based spatial representations and temporal features, the model demonstrates the ability to capture TSS variability across the spatially heterogeneous coastal environments evaluated in this study.

(2) Spatiotemporal patterns of TSS.

The reconstructed TSS dataset reveals a persistent "high-inshore, low-offshore" spatial pattern along China's coast, with pronounced regional differences among northern shallow seas, major estuarine systems, and southern coastal waters. A distinct seasonal cycle is identified, characterized by elevated TSS concentrations in winter and reduced concentrations in summer, reflecting the combined influences of hydrodynamic forcing and riverine sediment inputs.

(3) Interannual variability and regional evolution.

The reconstructed TSS dataset exhibits pronounced interannual variability during 2016–2025, with an increasing trend during 2016–2020 followed by a general decline after 2020. The magnitude of these changes varies considerably among different coastal regions, with stronger variability occurring in northern shallow seas and major estuaries, whereas the southern offshore waters remain comparatively stable.

Overall, the proposed STGNN-TSS framework provides an effective approach for large-scale, long-term TSS retrieval from satellite observations. The reconstructed TSS dataset offers valuable support for coastal environmental monitoring, suspended sediment dynamics analysis, and the sustainable management of China's coastal ecosystems.

Author Contributions: Conceptualization, Y.G. and Y.P.W.; methodology, Y.G. and J.R.; software, Y.G.; validation, Y.G. and H.S.; formal analysis, Y.G. and J.R.; investigation, Y.G., H.S. and C.Z.; data curation, Y.G.; writing—original draft preparation, Y.G.; writing—review and editing, Y.G., J.R., H.S., C.Z. and Y.P.W.; visualization, Y.G. and C.Z.; resources, Y.P.W.; supervision, Y.P.W.; project administration, Y.P.W.; funding acquisition, Y.P.W. All authors have read and agreed to the published version of the manuscript.

Funding: This research was funded by the National Natural Science Foundation of China (Grant No. 42293261) and the Postgraduate Research & Practice Innovation Program of Jiangsu Province (KYCX25_1231).

Data Availability Statement: The TSS dataset generated in this study is publicly available at https://doi.org/10.6084/m9.figshare.33174731 (accessed on 6 August 2026) under a Creative Commons Attribution 4.0 International (CC BY 4.0) license. The TSS observations used in this study were obtained from the National Marine Science Data Center and the National Science and Technology Resource Sharing Service Platform (https://mds.nmdis.org.cn/; accessed on 12 November 2025). The Sentinel-2 multispectral imagery time series used in this study were accessed through the Google Earth Engine platform (https://earthengine.google.com/; accessed on 25 December 2025).

Acknowledgments: The authors gratefully acknowledge the data support provided by the National Marine Science Data Center and the National Science and Technology Resource Sharing Service Platform (https://mds.nmdis.org.cn/). We are also thankful for the contributions made by Runtian Wang, a student who assisted with data organization and provided valuable assistance in this research. Generative artificial intelligence (GenAI), specifically ChatGPT (OpenAI, GPT-5.5), was used during manuscript preparation to improve the clarity and language of the text. The tool was not used to generate research data, conduct data analysis, design the study, or interpret the results. All AI-assisted content was carefully reviewed and edited by the authors, who take full responsibility for the content of this publication.

Conflicts of Interest: The authors declare no conflicts of interest.

References

1. Klemas, V.; Bartlett, D.; Philpot, W.; Rogers, R.; Reed, L. Coastal and Estuarine Studies with ERTS-1 and Skylab. *Remote Sens. Environ*. **1974**, *3*, 153–174. [CrossRef]
2. Myint, S.W.; Walker, N.D. Quantification of Surface Suspended Sediments along a River Dominated Coast with NOAA AVHRR and SeaWiFS Measurements: Louisiana, USA. *Int. J. Remote Sens*. **2002**, *23*, 3229–3249. [CrossRef]
3. Allen, J.R. Morphodynamics of Holocene Salt Marshes: A Review Sketch from the Atlantic and Southern North Sea Coasts of Europe. *Quat. Sci. Rev.* **2000**, *19*, 1155–1231. [CrossRef]
4. Schartau, M.; Riethmüller, R.; Flöser, G.; Van Beusekom, J.E.E.; Krasemann, H.; Hofmeister, R.; Wirtz, K. On the Separation between Inorganic and Organic Fractions of Suspended Matter in a Marine Coastal Environment. *Prog. Oceanogr.* **2019**, *171*, 231–250. [CrossRef]
5. van der Hout, C.M.; Witbaard, R.; Hoekstra, P.; Gerkema, T. Wind-Driven Variability in Longshore Transport of SPM in the Turbidity Maximum Zone along the Dutch Coast. *Cont. Shelf Res*. **2025**, *286*, 105421. [CrossRef]
6. Wen, Z.; Wang, Q.; Liu, G.; Jacinthe, P.-A.; Wang, X.; Lyu, L.; Tao, H.; Ma, Y.; Duan, H.; Shang, Y.; et al. Remote Sensing of Total Suspended Matter Concentration in Lakes across China Using Landsat Images and Google Earth Engine. *ISPRS J. Photogramm. Remote Sens*. **2022**, *187*, 61–78. [CrossRef]
7. Niu, C.; Tan, K.; Jia, X.; Wang, X. Deep Learning Based Regression for Optically Inactive Inland Water Quality Parameter Estimation Using Airborne Hyperspectral Imagery. *Environ. Pollut*. **2021**, *286*, 117534. [CrossRef] [PubMed]
8. Wu, J.; Lu, J. Spatial Scale Effects of Landscape Metrics on Stream Water Quality and Their Seasonal Changes. *Water Res*. **2021**, *191*, 116811. [CrossRef] [PubMed]

9. Chawla, I.; Karthikeyan, L.; Mishra, A.K. A Review of Remote Sensing Applications for Water Security: Quantity, Quality, and Extremes. *J. Hydrol.* **2020**, *585*, 124826. [CrossRef]
10. Luo, Y.; Doxaran, D.; Ruddick, K.; Shen, F.; Gentili, B.; Yan, L.; Huang, H. Saturation of Water Reflectance in Extremely Turbid Media Based on Field Measurements, Satellite Data and Bio-Optical Modelling. *Opt. Express* **2018**, *26*, 10435–10451. [CrossRef] [PubMed]
11. Rahman, M.M.; Shults, R.; Tiwari, S.P.; Arshad, A.; Usman, M.; Raihan, A.; Ishraque, M.F. Review on Sea Water Quality (SWQ) Monitoring Using Satellite Remote Sensing Techniques (SRST). *Mar. Pollut. Bull.* **2025**, *217*, 118108. [CrossRef] [PubMed]
12. Wirabumi, P.; Kamal, M.; Wicaksono, P. Determining Effective Water Depth for Total Suspended Solids (TSS) Mapping Using PlanetScope Imagery. *Int. J. Remote Sens.* **2021**, *42*, 5784–5810. [CrossRef]
13. Guo, H.; Zhu, X.; Jeanne Huang, J.; Zhang, Z.; Tian, S.; Chen, Y. An Enhanced Deep Learning Approach to Assessing Inland Lake Water Quality and Its Response to Climate and Anthropogenic Factors. *J. Hydrol.* **2023**, *620*, 129466. [CrossRef]
14. Zhai, Y.; Zhong, P.; Duan, H.; Zhang, D.; Chen, X.; Guo, X. Modeling of Suspended Particulate Matter Concentration in an Extremely Turbid River Based on Multispectral Remote Sensing from an Unmanned Aerial Vehicle (UAV). *Remote Sens.* **2023**, *15*, 5398. [CrossRef]
15. Jaywant, S.A.; Arif, K.M. Remote Sensing Techniques for Water Quality Monitoring: A Review. *Sensors* **2024**, *24*, 8041. [CrossRef] [PubMed]
16. Pahlevan, N.; Smith, B.; Alikas, K.; Anstee, J.; Barbosa, C.; Binding, C.; Bresciani, M.; Cremella, B.; Giardino, C.; Gurlin, D.; et al. Simultaneous Retrieval of Selected Optical Water Quality Indicators from Landsat-8, Sentinel-2, and Sentinel-3. *Remote Sens. Environ.* **2022**, *270*, 112860. [CrossRef]
17. Chen, Z.; Hu, C.; Muller-Karger, F. Monitoring Turbidity in Tampa Bay Using MODIS/Aqua 250-m Imagery. *Remote Sens. Environ.* **2007**, *109*, 207–220. [CrossRef]
18. Petus, C.; Marieu, V.; Novoa, S.; Chust, G.; Bruneau, N.; Froidefond, J.-M. Monitoring Spatio-Temporal Variability of the Adour River Turbid Plume (Bay of Biscay, France) with MODIS 250-m Imagery. *Cont. Shelf Res.* **2014**, *74*, 35–49. [CrossRef]
19. Moridnejad, A.; Abdollahi, H.; Alavipanah, S.K.; Samani, J.M.V.; Moridnejad, O.; Karimi, N. Applying Artificial Neural Networks to Estimate Suspended Sediment Concentrations along the Southern Coast of the Caspian Sea Using MODIS Images. *Arab. J. Geosci.* **2015**, *8*, 891–901. [CrossRef]
20. Chen, J.; Huang, J.; Zhang, X.; Chen, J.; Chen, X. Monitoring Total Suspended Solids Concentration in Poyang Lake via Machine Learning and Landsat Images. *J. Hydrol. Reg. Stud.* **2023**, *49*, 101499. [CrossRef]
21. Torres-Vera, M.A. Mapping of Total Suspended Solids Using Landsat Imagery and Machine Learning. *Int. J. Environ. Sci. Technol.* **2023**, *20*, 11877–11890. [CrossRef]
22. Wu, G.; Cui, L.; Liu, L.; Chen, F.; Fei, T.; Liu, Y. Statistical Model Development and Estimation of Suspended Particulate Matter Concentrations with Landsat 8 OLI Images of Dongting Lake, China. *Int. J. Remote Sens.* **2015**, *36*, 343–360. [CrossRef]
23. Zhang, M.; Dong, Q.; Cui, T.; Xue, C.; Zhang, S. Suspended Sediment Monitoring and Assessment for Yellow River Estuary from Landsat TM and ETM plus Imagery. *Remote Sens. Environ.* **2014**, *146*, 136–147. [CrossRef]
24. Pahlevan, N.; Chittimalli, S.K.; Balasubramanian, S.V.; Vellucci, V. Sentinel-2/Landsat-8 Product Consistency and Implications for Monitoring Aquatic Systems. *Remote Sens. Environ.* **2019**, *220*, 19–29. [CrossRef]
25. Feng, L.; Hou, X.; Zheng, Y. Monitoring and Understanding the Water Transparency Changes of Fifty Large Lakes on the Yangtze Plain Based on Long-Term MODIS Observations. *Remote Sens. Environ.* **2019**, *221*, 675–686. [CrossRef]
26. Li, P.; Ke, Y.; Bai, J.; Zhang, S.; Chen, M.; Zhou, D. Spatiotemporal Dynamics of Suspended Particulate Matter in the Yellow River Estuary, China during the Past Two Decades Based on Time-Series Landsat and Sentinel-2 Data. *Mar. Pollut. Bull.* **2019**, *149*, 110518. [CrossRef] [PubMed]
27. Luo, W.; Shen, F.; He, Q.; Cao, F.; Zhao, H.; Li, M. Changes in Suspended Sediments in the Yangtze River Estuary from 1984 to 2020: Responses to Basin and Estuarine Engineering Constructions. *Sci. Total Environ.* **2022**, *805*, 150381. [CrossRef] [PubMed]
28. Sun, Q.; Luo, W.; Dong, X.; Lei, S.; Mu, M.; Zeng, S. Landsat Observations of Total Suspended Solids Concentrations in the Pearl River Estuary, China, over the Past 36 Years. *Environ. Res.* **2024**, *249*, 118461. [CrossRef] [PubMed]
29. Balasubramanian, S.V.; Pahlevan, N.; Smith, B.; Binding, C.; Schalles, J.; Loisel, H.; Gurlin, D.; Greb, S.; Alikas, K.; Randla, M.; et al. Robust Algorithm for Estimating Total Suspended Solids (TSS) in Inland and Nearshore Coastal Waters. *Remote Sens. Environ.* **2020**, *246*, 111768. [CrossRef]
30. Estournel, C.; Mikolajczak, G.; Ulses, C.; Bourrin, F.; Canals, M.; Charmasson, S.; Doxaran, D.; Duhaut, T.; de Madron, X.D.; Marsaleix, P.; et al. Sediment Dynamics in the Gulf of Lion (NW Mediterranean Sea) during Two Autumn–Winter Periods with Contrasting Meteorological Conditions. *Prog. Oceanogr.* **2023**, *210*, 102942. [CrossRef]
31. Jiang, D.; Matsushita, B.; Pahlevan, N.; Gurlin, D.; Lehmann, M.K.; Fichot, C.G.; Schalles, J.; Loisel, H.; Binding, C.; Zhang, Y.; et al. Remotely Estimating Total Suspended Solids Concentration in Clear to Extremely Turbid Waters Using a Novel Semi-Analytical Method. *Remote Sens. Environ.* **2021**, *258*, 112386. [CrossRef]

32. Tao, H.; Song, K.; Wen, Z.; Liu, G.; Shang, Y.; Fang, C.; Wang, Q. Remote Sensing of Total Suspended Matter of Inland Waters: Past, Current Status, and Future Directions. *Ecol. Inform.* **2025**, *86*, 103062. [CrossRef]
33. Yu, X.; Lee, Z.; Shen, F.; Wang, M.; Wei, J.; Jiang, L.; Shang, Z. An Empirical Algorithm to Seamlessly Retrieve the Concentration of Suspended Particulate Matter from Water Color across Ocean to Turbid River Mouths. *Remote Sens. Environ.* **2019**, *235*, 111491. [CrossRef]
34. Anand, V.; Oinam, B.; Wieprecht, S. Machine Learning Approach for Water Quality Predictions Based on Multispectral Satellite Imageries. *Ecol. Inform.* **2024**, *84*, 102868. [CrossRef]
35. Zheng, H.; Hou, S.; Liu, J.; Xiong, Y.; Wang, Y. Advanced Machine Learning and Water Quality Index (WQI) Assessment: Evaluating Groundwater Quality at the Yopurga Landfill. *Water* **2024**, *16*, 1666. [CrossRef]
36. Guo, S.; Lin, Y.; Feng, N.; Song, C.; Wan, H. Attention Based Spatial-Temporal Graph Convolutional Networks for Traffic Flow Forecasting. In Proceedings of the AAAI Conference on Artificial Intelligence, Honolulu, HI, USA, 27 January–1 February 2019; Volume 33, pp. 922–929.
37. Kawabata, T.; Toda, H. Exploring of STGNN for Traffic Forecasting at Expanding Traffic Network. In *Database and Expert Systems Applications*; Lecture Notes in Computer Science; Strauss, C., Amagasa, T., Manco, G., Kotsis, G., Tjoa, A.M., Khalil, I., Eds.; Springer Nature: Cham, Switzerland, 2024; Volume 14911, pp. 116–121.
38. Yang, Y.; Liu, Y.; Zhang, Y.; Shu, S.; Zheng, J. DEST-GNN: A Double-Explored Spatio-Temporal Graph Neural Network for Multi-Site Intra-Hour PV Power Forecasting. *Appl. Energy* **2025**, *378*, 124744. [CrossRef]
39. Yin, J.; Qiu, A.; Fang, L.; Wang, N.; Dong, C.; Ge, S. STGNN: A Novel Spatial-Temporal Graph Neural Network for Predicting Complicated Business Process Performance under Multi-Event Parallelism. *Expert Syst. Appl.* **2025**, *291*, 128391. [CrossRef]
40. Yu, Y.; Liu, Q. Unified TKG-STGCN Framework for Grid Fault and FDI Defense. *Measurement* **2025**, *259*, 119660. [CrossRef]
41. Fofanah, A.J.; Chen, D.; Wen, L.; Zhang, S. Addressing Imbalance in Graph Datasets: Introducing Gate-Gnn with Graph Ensemble Weight Attention and Transfer Learning for Enhanced Node Classification. *Expert Syst. Appl.* **2024**, *255*, 124602. [CrossRef]
42. He, J.; Tanyas, H.; Huang, D.; Lombardo, L. Space-Time Explainable Modelling of Regional Hillslope Deformation, an Example from the Tibetan Plateau. *Remote Sens. Environ.* **2025**, *329*, 114924. [CrossRef]
43. Ławryńczuk, M.; Zarzycki, K. LSTM and GRU Type Recurrent Neural Networks in Model Predictive Control: A Review. *Neurocomputing* **2025**, *632*, 129712. [CrossRef]
44. Liu, X.; Wang, M. High Spatial Resolution Gap-Free Global and Regional Ocean Color Products. *IEEE Trans. Geosci. Remote Sens.* **2023**, *61*, 1–18. [CrossRef]
45. Gohin, F. Annual Cycles of Chlorophyll-*a*, Non-Algal Suspended Particulate Matter, and Turbidity Observed from Space and in-Situ in Coastal Waters. *Ocean Sci.* **2011**, *7*, 705–732. [CrossRef]
46. Wang, H.; Wang, A.; Bi, N.; Zeng, X.; Xiao, H. Seasonal Distribution of Suspended Sediment in the Bohai Sea, China. *Cont. Shelf Res.* **2014**, *90*, 17–32. [CrossRef]
47. Zhan, W.; Wu, J.; Wei, X.; Tang, S.; Zhan, H. Spatio-Temporal Variation of the Suspended Sediment Concentration in the Pearl River Estuary Observed by MODIS during 2003–2015. *Cont. Shelf Res.* **2019**, *172*, 22–32. [CrossRef]
48. Yang, Y.-P.; Zhang, M.-J.; Li, Y.-T.; Zhang, W. The Variations of Suspended Sediment Concentration in Yangtze River Estuary. *J. Hydrodyn. Ser. B* **2015**, *27*, 845–856. [CrossRef]
49. Zhao, G.; Jiang, W.; Wang, T.; Chen, S.; Bian, C. Decadal Variation and Regulation Mechanisms of the Suspended Sediment Concentration in the Bohai Sea, China. *JGR Oceans* **2022**, *127*, e2021JC017699. [CrossRef]

Disclaimer/Publisher's Note: The statements, opinions and data contained in all publications are solely those of the individual author(s) and contributor(s) and not of MDPI and/or the editor(s). MDPI and/or the editor(s) disclaim responsibility for any injury to people or property resulting from any ideas, methods, instructions or products referred to in the content.